

A Robust Nonparametric Framework for Detecting Repeated Spatial Patterns

Rajitha Senanayake^a, Pratheepa Jeganathan^{a,b}

^a*Department of Mathematics and Statistics, McMaster University, Hamilton, Ontario, Canada*

^b*School of Computational Science and Engineering, McMaster University, Hamilton, Ontario, Canada*

Abstract

Identifying spatially contiguous clusters and repeated spatial patterns (RSP) characterized by similar underlying distributions that are spatially apart is a key challenge in modern spatial statistics. Existing constrained clustering methods enforce spatial contiguity but are limited in their ability to identify RSP. We propose a novel nonparametric framework that addresses this limitation by combining constrained clustering with a post-clustering reassignment step based on the maximum mean discrepancy (MMD) statistic. We employ a block permutation strategy within each cluster that preserves local attribute structure when approximating the null distribution of the MMD. We also show that the MMD^2 statistic is asymptotically consistent under second-order stationarity and spatial mixing conditions. This two-stage approach enables the detection of clusters that are both spatially distant and similar in distribution. Through simulation studies that vary spatial dependence, cluster sizes, shapes, and multivariate dimensionality, we demonstrate the robustness of our proposed framework in detecting RSP. We further illustrate its applicability through an analysis of spatial proteomics data from patients with triple-negative breast cancer. Overall, our framework presents a methodological advancement in spatial clustering, offering a flexible and robust solution for spatial datasets that exhibit repeated patterns.

Keywords:

Constrained clustering, Repeated spatial patterns, Maximum mean discrepancy, Block permutation, Spatial Omics

1. Introduction

Spatial clustering refers to identifying regions that exhibit similarity in their spatial distribution. Typically, spatial clusters are contiguous, as locations in close proximity tend to share similar attribute values. However, similar spatial patterns can also emerge repeatedly in distant locations, forming discrete patches referred to as repeated spatial clusters (RSP). These may reflect shared underlying processes such as climate patterns (Benevento and Durante, 2024), socioeconomic trends (Murtagh, 1985), and disease dynamics (Kulldorff, 1997). Despite the relevance of RSP detection in practical applications, many existing spatial clustering methods are limited in their capacity to identify RSP.

One domain that increasingly relies on spatial clustering is spatial omics. Recent advances in spatial technology have greatly expanded the ability to study biological complexity within tissues. Reflecting this impact, spatial proteomics was named the 2024 Method of the Year by Nature Methods (Editorial Board, 2024). These developments have increased the need for robust spatial clustering methods that can accommodate the heterogeneous nature of spatial omics data. Such data may consist of continuous measurements (e.g., protein marker intensities, gene expression levels), categorical annotations (e.g., cell type classifications), or binary indicators (e.g., presence or absence of specific markers). Consequently, spatial clustering methods must be flexible enough to handle any of these data types, making them one of the tools to uncover spatio-temporal patterns by integrating multimodal data from the Human Tumor Atlas Network (HTAN) (de Bruijn et al., 2025).

Several methods have been developed for clustering spatial omics data. For example, Giotto identifies spatially homogeneous regions by modeling gene expression patterns using a hidden Markov random field (HMRF) (Dries et al., 2021). Moreover, Banksy uses k-means clustering, Leiden community detection, or many other algorithms, with spatial information encoded as node attributes derived from azimuthal Gabor filters (AGFs) that capture local spatial structure (Singhal et al., 2024). Proust employs a graph-based autoencoder to learn hybrid feature representations that integrate gene expression and spatial proximity, followed by nonparametric or model-based clustering on the learned embeddings to identify spatial domains (Yao et al., 2024).

While methods such as Giotto, Banksy, and Proust leverage graph-based spatial representations or enhanced feature embeddings for spatial domain detection, they exhibit limitations in handling certain data modalities and RSP. For instance, the HMRF framework in Giotto models gene expression patterns and can

identify spatial patches with similar expression distributions that may align with RSP. However, it is not directly applicable to categorical or binary data. Banksy and Proust, on the other hand, may fail to capture RSP, particularly in the presence of varying spatial dependence or irregular spatial shapes.

Spatial clustering methods can be broadly categorized into three types: (1) attribute-based methods, (2) integrated methods that consider both attribute similarity and spatial proximity, and (3) methods that explicitly balance these two components to detect RSP. Attribute-based methods, such as k-means and hierarchical clustering, primarily focus on clustering based on attribute similarity. These methods can incorporate spatial information by treating coordinates as additional attributes or by enhancing spatial representation, such as splines or Gabor filters. While they are typically nonparametric and flexible across diverse data types, they often fail to ensure spatial contiguity. Integrated methods, including constrained hierarchical clustering (CHC) and scan statistic-based clustering, combine spatial proximity with attribute similarity to identify spatially contiguous clusters (Guénard and Legendre, 2022; Miranda et al., 2017; Ester et al., 1996). The CHC explicitly incorporates spatial constraints to ensure contiguity, whereas scan statistics detect regions with significantly higher attribute densities than expected under a null model, assessing statistical significance (Abolhassani and Prates, 2021). Despite their utility, these integrated methods may struggle to identify RSP because they weigh spatial proximity and attribute similarity differently.

To address the above limitation, the methods that counterbalances spatial and attribute contributions have emerged. The STICC method constructs subregions using Gaussian Markov random fields and employs a mixture modeling framework to assign these subregions to clusters (Kang et al., 2022). STICC can detect RSP by clustering subregions that are spatially contiguous and RSP. However, its reliance on Gaussian assumptions and the combinatorial complexity of the subregion-to-cluster assignment procedure may limit its applicability to non-Gaussian data types and large-scale spatial omics datasets.

RSPs have also been explored in the spatio-temporal clustering literature. For example, the Spatial-CHC algorithm constructs a temporal correlation matrix using Gaussian rank correlation and a spatial correlation matrix based on a Matérn covariance function. These matrices are combined into a single dissimilarity matrix by computing a geodesic average on the Riemannian manifold of correlation matrices. Hierarchical clustering is then applied to this combined dissimilarity matrix to identify spatial patterns that recur over time (Benevento and Durante, 2024). However, this approach is specifically designed to capture temporal repetition of spatial patterns, rather than RSP within a spatial domain.

While parametric approaches such as STICC offer a data-generative process well-suited for detecting RSP, their limitations motivate our development of a more flexible, nonparametric framework. The method proceeds in two stages: it first applies constrained clustering to ensure spatial contiguity, followed by a post-clustering comparison to identify regions that share similar spatial distribution. The framework is broadly applicable and can be paired with any constrained clustering method to detect RSP within the spatial domain.

Our main contribution is a novel post-clustering framework, repSpat, designed to identify RSP by addressing the common over-segmentation produced by constrained clustering methods. Specifically, we introduce multiple hypotheses testing approach that (1) quantifies similarity in distributions between clusters using the maximum mean discrepancy (MMD) statistic, which is well suited for detecting general differences in multivariate distributions (Gretton et al., 2006); and (2) employs a block permutation strategy that preserves local spatial structure within clusters, enabling valid inference under these unknowns (Guillot and Rousset, 2013). This combination allows repSpat to reassign labels to spatially distant clusters that arise from similar underlying spatial processes, extending the utility of existing constrained clustering methods to settings with RSP.

The remainder of the paper is organized as follows. Section 2 describes the proposed methodology, repSpat, in detail. Section 3 presents a simulation study evaluating the performance of repSpat under varying conditions and comparing these results with those obtained from Banksy. Section 4 demonstrates the application of our approach to spatial proteomics data. Finally, Section 5 concludes with a discussion and future directions.

2. Methodology

Let $X(s)$ denote a multivariate spatial process, where $s \in \mathcal{S} \subseteq \mathbb{R}^2$ is a spatial location in a continuous or discrete domain \mathcal{S} , and $X(s) \in \mathcal{X} \subseteq \mathbb{R}^p$ is a p -dimensional attribute vector observed at s . Let s_1, \dots, s_n denote a set of n spatial sampling locations. Based on observations $X(s_1), \dots, X(s_n)$, we define an attribute-based dissimilarity matrix \mathbf{D} , where each entry d_{ij} represents the dissimilarity between the observations at locations s_i and s_j .

To incorporate spatial constraints in clustering, we define spatial links ℓ_{ij} based on the neighborhood structure among the spatial locations s_1, \dots, s_n , where $i, j \in 1, \dots, n$. These spatial links may be derived from adjacency, distance thresholds, or empirical spatial dependence measures.

We now introduce the repSpat framework, which is designed to detect repeated spatial patterns in $X(s)$ through the following four steps.

2.1. Constrained Clustering

We employ constrained agglomerative hierarchical clustering (CAHC) to identify spatially contiguous clusters (Guénard and Legendre, 2022). CAHC begins by assigning each observation $X(s_i)$ to its own cluster. At each step, it merges the pair of clusters with the smallest attribute-based dissimilarity d_{ij} , subject to a spatial contiguity constraint. This process continues until either all observations are grouped into a single connected cluster or constraints are met. To accelerate merging, we use the Lance–Williams distance update formula (Lance and Williams, 1967).

CAHC requires two tuning parameters: (1) the number of nearest neighbors used to define spatial links, and (2) the number of clusters. These parameters jointly influence spatial distortion in cluster identification, which we define as the degree to which the derived subregions exhibit stationary spatial processes within each cluster. That is, within each cluster, the mean function is constant, and the covariance depends only on spatial lag. Notably, observations within each cluster may exhibit repeated or structured patterns, driven by spatial proximity, attribute similarity, or hierarchical organization.

The silhouette score is a widely used metric for evaluating clustering quality, based on the trade-off between within-cluster cohesion and between-cluster separation (Rousseeuw, 1987). A higher silhouette score indicates that clusters are both compact and well-separated. We adapt this metric to incorporate spatial links ℓ_{ij} , yielding a spatially-informed silhouette score that guides the selection of the two tuning parameters in CAHC.

Suppose CAHC produces G clusters, denoted by $C^{(1)}, \dots, C^{(G)}$. For a spatial location $i \in C^{(g)}$, the average within-cluster dissimilarity is defined as

$$a(i) = \frac{1}{n_g - 1} \sum_{j \in C^{(g)} j \neq i} d_{ij}, \quad (1)$$

where $n_g = |C^{(g)}|$ is the number of points in cluster $C^{(g)}$.

To compute the average between-cluster dissimilarity, we restrict comparisons to clusters that are spatially adjacent to $C^{(g)}$ -i.e., those sharing at least one spatial link with it. The modified between-cluster dissimilarity for point i is given by

$$b(i) = \min_{C^{(\ell)} \neq C^{(g)}: \ell_{g\ell}=1} \left(\frac{1}{|C^{(\ell)}|} \sum_{j \in C^{(\ell)}} d_{ij} \right), \quad (2)$$

where $\ell_{g\ell} = 1$ indicates at least one spatial link exists between any point in $C^{(g)}$ and any point in $C^{(\ell)}$.

The spatially-informed silhouette score for point i is then

$$sh(i) = \frac{b(i) - a(i)}{\max a(i), b(i)}. \quad (3)$$

This modified silhouette score provides a more accurate assessment of clustering quality in the spatial setting by jointly evaluating cluster compactness and separation, while respecting spatial constraints.

We now turn to assessing whether the clusters identified by CAHC exhibit RSP. To this end, we define a multiple hypotheses testing procedure based on the maximum mean discrepancy (MMD) statistic.

2.2. Testing for Repeated Spatial Patterns (RSP) Across Clusters

Given G clusters obtained from CAHC using a selected neighborhood size m , we assess whether any pair of clusters shares a similar spatial distribution to identify RSP.

Let $C^{(g)} = \{\mathbf{s}_1^{(g)}, \dots, \mathbf{s}_{n_g}^{(g)}\}$ and $C^{(h)} = \{\mathbf{s}_1^{(h)}, \dots, \mathbf{s}_{n_h}^{(h)}\}$ denote two such clusters, each corresponding to a spatial subregion. The associated multivariate attributes are given by $\mathbf{X}^{(g)} = \{X(\mathbf{s}_i^{(g)}) \in \mathbb{R}^p : i = 1, \dots, n_g\}$ and $\mathbf{X}^{(h)} = \{X(\mathbf{s}_j^{(h)}) \in \mathbb{R}^p : j = 1, \dots, n_h\}$. Let $P^{(g)}$ and $P^{(h)}$ denote the joint distributions of $\mathbf{X}^{(g)}$ and $\mathbf{X}^{(h)}$, respectively. Assuming that each $\mathbf{X}^{(g)}$ is second-order stationary, we test the null hypothesis $H_0 : P^{(g)} = P^{(h)}$ and the alternative is that $H_A : P^{(g)} \neq P^{(h)}$.

To test this hypothesis, we employ a nonparametric test statistic, the maximum mean discrepancy (MMD), which measures the difference between $P^{(g)}$ and $P^{(h)}$ based on their embeddings in a reproducing kernel Hilbert space (RKHS) (Gretton et al., 2006). We now formally define the RKHS and the squared MMD statistic, MMD^2 .

We follow the definition of RKHS given in (Berlinet and Thomas-Agnan, 2011, pp. 6–9). Let $k : \mathcal{X} \times \mathcal{X} \rightarrow \mathbb{R}$ be a positive definite kernel, where $\mathcal{X} \subseteq \mathbb{R}^p$. The RKHS, \mathcal{H}_k associated with k is a Hilbert space of functions $f : \mathcal{X} \rightarrow \mathbb{R}$ such that, for each $\mathbf{x} \in \mathcal{X}$, the evaluation functional $\mathcal{F}_{\mathbf{x}} : \mathcal{H}_k \rightarrow \mathbb{R}$, defined by $\mathcal{F}_{\mathbf{x}}(f) = f(\mathbf{x})$, is bounded and linear. By Riesz's representation theorem, there exists a unique representer $k(\cdot, \mathbf{x}) \in \mathcal{H}_k$ such that the reproducing property holds: $f(\mathbf{x}) = \langle f, k(\cdot, \mathbf{x}) \rangle_{\mathcal{H}_k}$. This property also implies that for any $\mathbf{x}, \mathbf{y} \in \mathcal{X}$, the kernel function satisfies $k(\mathbf{x}, \mathbf{y}) = \langle k(\cdot, \mathbf{x}), k(\cdot, \mathbf{y}) \rangle_{\mathcal{H}_k}$.

We now define the MMD^2 between the distributions $P^{(g)}$ and $P^{(h)}$ in \mathcal{H}_k , following Gretton et al. (2006):

$$\text{MMD}^2(P^{(g)}, P^{(h)}; \mathcal{H}_k) = \|\mu_{P^{(g)}} - \mu_{P^{(h)}}\|_{\mathcal{H}_k}^2, \quad (4)$$

where $\mu_{P^{(g)}} := \mathbb{E}_{\mathbf{x} \sim P^{(g)}} [k(\cdot, \mathbf{x})]$ and $\mu_{P^{(h)}} := \mathbb{E}_{\mathbf{x} \sim P^{(h)}} [k(\cdot, \mathbf{x})]$ are the kernel mean embeddings of $P^{(g)}$ and $P^{(h)}$ in \mathcal{H}_k , respectively. The properties of the mean embeddings are studied in Muandet et al. (2017).

Given observed samples $\mathbf{x}^{(g)} = \{\mathbf{x}_i^{(g)}\}_{i=1}^{n_g}$ and $\mathbf{x}^{(h)} = \{\mathbf{x}_j^{(h)}\}_{j=1}^{n_h}$ drawn from $P^{(g)}$ and $P^{(h)}$, respectively, the empirical estimate of MMD^2 is given by

$$\begin{aligned} \widehat{\text{MMD}}^2(X^{(g)}, X^{(h)}; \mathcal{H}_k) &= \frac{1}{n_g^2} \sum_{i=1}^{n_g} \sum_{j=1}^{n_g} k(\mathbf{x}_i^{(g)}, \mathbf{x}_j^{(g)}) + \frac{1}{n_h^2} \sum_{i=1}^{n_h} \sum_{j=1}^{n_h} k(\mathbf{x}_i^{(h)}, \mathbf{x}_j^{(h)}) \\ &\quad - \frac{2}{n_g n_h} \sum_{i=1}^{n_g} \sum_{j=1}^{n_h} k(\mathbf{x}_i^{(g)}, \mathbf{x}_j^{(h)}). \end{aligned} \quad (5)$$

The kernel function computes a measure of similarity between two vectors by implicitly evaluating their inner product in a high-dimensional feature space. For k to be a valid reproducing kernel, it must satisfy Mercer's conditions: it must be symmetric, continuous, and yield a positive semi-definite kernel matrix (Muandet et al., 2017, Theorem 2.1). Many radial basis function (RBF) kernels, such as the Gaussian kernel, define similarity based on the Euclidean distance $\|\mathbf{x} - \mathbf{y}\|$, directly into the kernel evaluation. For multivariate binary attributes, Euclidean distance may be replaced with the Jaccard distance. Table 1 summarizes the three kernels investigated in this study, all of which evaluate similarity between observations $\mathbf{x}, \mathbf{y} \in \mathcal{X}$, given an appropriate choice of distance matrix tailored to the data type.

In Appendix D, we conducted simulations by varying the number of spatial points n , attribute dimension p , spatial autocorrelation η , kernel type, and kernel-specific parameters to investigate the sampling distribution of the MMD^2 statistic under scenarios where the underlying distributions of two clusters are either identical or different. In Figures D.10-D.12, we found that the inverse multiquadratic (IMQ) kernel with shape parameter $c \geq 1$ shifts the distribution of MMD^2 further away from zero when the cluster distributions differ, thereby enhancing sensitivity.

The kernel parameter (e.g., bandwidth in Gaussian and Laplacian kernels, shape parameter in the IMQ kernel) influences the power of the MMD^2 test under the alternative hypothesis by controlling the kernel's sensitivity to differences in distributions. In high-dimensional settings with multivariate attributes, larger kernel parameters are often necessary. This is because, as dimensionality increases,

Table 1: Three kernel functions based on the Euclidean distance $\|\mathbf{x} - \mathbf{y}\|$. The parameters σ and c are kernel-specific bandwidth or shape parameters.

Kernel	Formula
Gaussian (RBF) kernel	$\exp(-\ \mathbf{x} - \mathbf{y}\ ^2/\sigma^2)$
Laplacian kernel	$\exp(-\ \mathbf{x} - \mathbf{y}\ _1/\sigma)$
Inverse multiquadratic (IMQ) kernel	$(\ \mathbf{x} - \mathbf{y}\ _2^2 + c^2)^{-1/2}$

pairwise distances between observations tend to grow, causing kernel similarity values to shrink toward zero and reducing the ability to distinguish between distributions.

To address this, the kernel parameter should be scaled relative to the distribution of pairwise distances. For instance, in Figures D.14 - D.15 and Figures D.16-D.17, the Gaussian and Laplacian kernels requires a bandwidth σ that is at least 2 to avoid near zero kernel values for the simulated data in Section 3.1. Similarly, for the IMQ kernel, the parameter c should be set to balance attenuation of long-range distances while preserving sensitivity to meaningful local variation. Thus, appropriate kernel parameter selection is critical for maintaining test power, especially in high-dimensional or sparse-feature regimes, or when the distance measure is not normalized to lie within $[0, 1]$.

Note that the MMD^2 statistic in (5) is biased, but consistent when the observations in $\mathbf{x}^{(g)}$ and $\mathbf{x}^{(h)}$ are independent samples from $P^{(g)}$ and $P^{(h)}$, respectively (Gretton et al., 2006, Theorem 4). Next, we show that MMD^2 is consistent under spatial dependence.

Under the null hypothesis, we assume that the spatial processes $\mathbf{X}^{(g)}$ and $\mathbf{X}^{(h)}$ within clusters $\mathcal{C}^{(g)}$ and $\mathcal{C}^{(h)}$ are second-order stationary and $\mathcal{C}^{(g)}$ and $\mathcal{C}^{(h)}$ are disjoint. In Appendix C, we show that the unbiased version of (5) is asymptotically consistent under the model-free mixing condition of $\mathbf{X}^{(g)}$ and $\mathbf{X}^{(h)}$. Consequently, under the same condition, it follows that the biased version in (5) is also asymptotically consistent.

As demonstrated in our simulation study, the variance of the MMD^2 statistic remains finite even as the strength of spatial autocorrelation increases from weak to strong levels (see Figures D.11 and D.12). These results highlight the suitability of MMD^2 for analyzing the cluster results from the CAHC.

2.3. Block Permutation

Motivated by Mantel’s test for spatial clustering (Schabenberger and Gotway, 2017, pp. 14–16), recommendations for structure-preserving resampling in spatial data (Guillot and Rousset, 2013), and subsampling over the subregion to compute variance of the statistic (Sherman, 1996), we propose a block permutation approach to approximate the null distribution of the MMD^2 statistic.

Under the null hypothesis that $\mathbf{X}^{(g)} \sim \mathbf{X}^{(h)}$, the MMD^2 statistic in (5) is expected to be small. Standard permutation tests rely on the assumption that observations are exchangeable under the null. However, in our context, observations $\mathbf{X}^{(g)}$ and $\mathbf{X}^{(h)}$ may exhibit spatial or structural dependencies, such as local RSP within clusters. In particular, the kernel similarity $k(\mathbf{x}_i^{(g)}, \mathbf{x}_j^{(g)})$ may capture local attribute similarity that would be disrupted if individual observations were randomly permuted. For instance, if $\mathbf{x}_j^{(g)}$ is locally similar to $\mathbf{x}_i^{(g)}$ but is replaced with a randomly selected $\mathbf{x}_k^{(g)}$, the similarity $k(\mathbf{x}_i^{(g)}, \mathbf{x}_k^{(g)})$ may not preserve the same structure that leads to invalid approximations of the null distribution.

To address this, we partition each cluster $C^{(g)}$ and $C^{(h)}$ into blocks based on attribute similarity using the k -means clustering algorithm. Because the clusters identified by constrained clustering are already assumed to be approximately spatially proximal, we do not impose additional spatial constraints when forming blocks based on attribute similarity. If the CAHC clustering step retains the dendrogram, block definitions can also be derived by cutting the dendrogram at a fixed height within each cluster without requiring additional clustering.

Once blocks are defined, entire blocks are permuted between $C^{(g)}$ and $C^{(h)}$ to approximate the sampling distribution of $\widehat{\text{MMD}}^2$ under the null. Our method is conceptually related to structured resampling methods such as shift permutations (Guillot and Rousset, 2013), which aim to preserve spatial dependence when generating null distributions. The detailed block permutation procedure for testing between clusters $C^{(g)}$ and $C^{(h)}$ is outlined in Appendix A.

For each hypothesis test, the observed statistic $\text{MMD}_{\text{obs}}^2$ is compared against the null distribution obtained via block permutation. To account for multiple testing across all distinct cluster pairs identified by CAHC, we apply the Benjamini–Hochberg procedure to control the false discovery rate (FDR) at a threshold of 0.05 (Benjamini and Hochberg, 1995). Finally, repStat reassigns cluster labels based on the pairwise hypothesis tests.

2.4. Reassigning the Cluster Labels

To guide the final reassignment step, we adopt a graph-based approach in which each node represents a cluster obtained from CAHC, and an edge represents a pair of clusters for which there is not enough evidence to conclude that their distributions differ. Each edge is labeled with the corresponding observed $\text{MMD}_{\text{obs}}^2$ value.

As a rule of thumb, clusters that form fully connected subgraphs (cliques) are reassigned to a common label. When fully connected subgraphs do not form, the reassignment decision can be guided by the magnitude of the $\text{MMD}_{\text{obs}}^2$ values with smaller values indicating higher similarity between clusters. Figure B.9 illustrates an example of the reassignment procedure.

We now evaluate the performance of the proposed repStat framework using simulation studies designed to assess its ability to detect RSP under varying spatial dependence structures and cluster configurations.

3. Simulation Study

3.1. Simulation Settings

We conduct simulation studies to evaluate the performance of repStat in detecting RSP. In addition to assessing its ability to identify RSP, we examine the false discovery rate (FDR) control of the MMD^2 test when paired with block permutation. We also compare the clustering accuracy of repStat with that of Banksy, which can detect RSP when appropriately tuned for spatial neighborhood features.

The simulations vary the number of observations (n), the dimensionality of the multivariate attributes (p), and the strength of spatial dependence (η). While repStat is applicable to spatial processes defined over continuous or discrete domains, we simulate data from a Gaussian Markov random field (GMRF) to control simulation settings through model parameters. In each setting, p multivariate attributes are simulated independently from a mixture of conditional autoregressive (CAR) models.

Following Besag (1974), for a finite number of locations n , the joint distribution for one attribute $\mathbf{X}(s) = (X(s_1), X(s_2), \dots, X(s_n))^T$ is

$$\mathbf{X}(s) \sim \text{Normal}_n(\boldsymbol{\mu}, (\mathbf{I}_n - \mathbf{C})^{-1}\mathbf{M}), \quad (6)$$

where $\boldsymbol{\mu}$ is the $n \times 1$ mean vector, \mathbf{I}_n is the $n \times n$ identity matrix, and $\mathbf{M} = \text{diag}(\tau_1^2, \dots, \tau_n^2)$ is a diagonal matrix of variances assuming $\tau_i^2 = \tau^2$, $\forall i$. More-

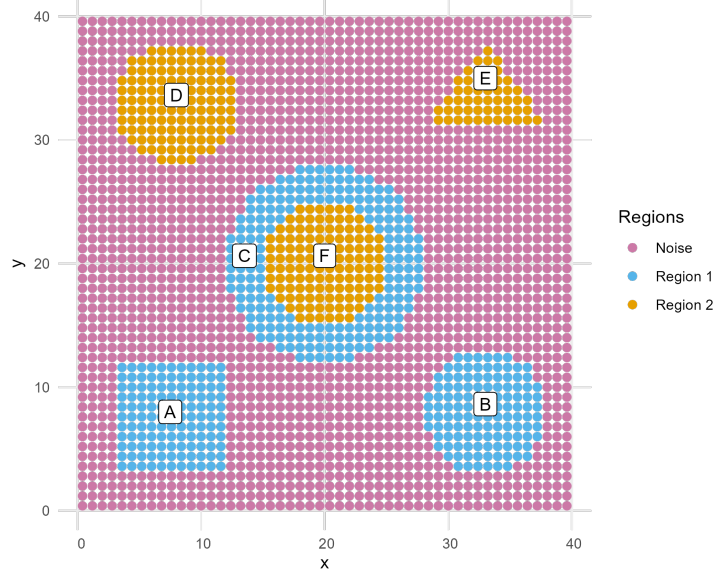


Figure 1: Simulation setup with 2500 spatial locations. Repeated spatial patterns are generated as Region 1 and Region 2, each comprising three patches. The remaining area is a noise region.

over, we assume isotropic dependence such that $\mathbf{C} = \eta \mathbf{W}$, where ρ is the spatial autocorrelation parameter and \mathbf{W} is the spatial weight matrix.

Spatial coordinates are simulated over a square domain $[0, 40] \times [0, 40]$, allowing infill asymptotic. Figure 1 shows an example configuration with $n = 2500$, containing six distinct regions (labeled A through F), which include circles, a triangle, a rectangle, and a donut-shaped region (comprising inner and outer circles). Within each region, spatial attributes $X(s)$ are independently generated for p attributes using the CAR model in (6), with region-specific parameters designed to produce RSP.

In Figure 1, patches A, B, and C share the same parameters and form Region 1; patches D, E, and F form Region 2 with a different set of parameters. For Region 1, we use mean $\boldsymbol{\mu}_1 = 4\mathbf{1}_{n_1}$ and variance $\tau_1^2 = 1$; for Region 2, we use mean $\boldsymbol{\mu}_2 = 10\mathbf{1}_{n_2}$ and variance $\tau_2^2 = 1$. All six patches share an 8-nearest neighbor spatial weight matrix and the same autocorrelation parameter η . To account for background noise, we include an additional noise region, where the realizations are drawn from a standard Gaussian distribution with mean 0 and variance 1.

We perform 100 simulation runs for each of the following combinations: $n \in \{2500, 4900\}$, $p \in \{5, 10\}$, and $\eta \in \{0.3, 0.8\}$. We use the inverse multiquadric

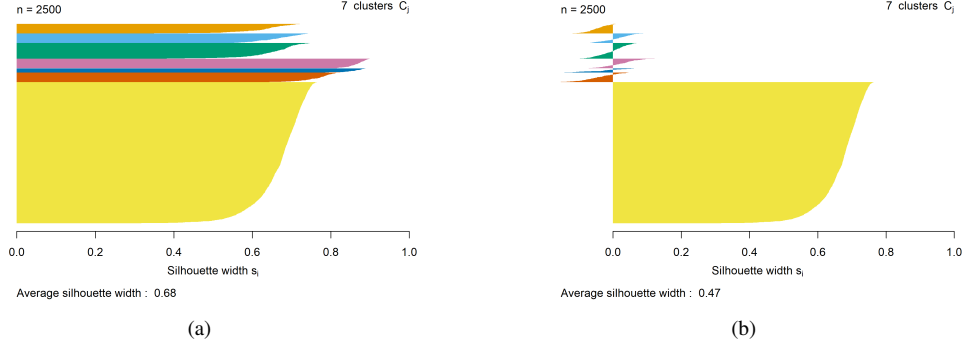


Figure 2: Comparison of silhouette scores for a representative simulation run with $n = 2500$, $p = 5$, and $\eta = 0.8$. a) Modified silhouette score incorporating spatial links; (b) Standard silhouette score.

(IMQ) kernel with $c = 1$ to compute MMD^2 , but larger than 1 can increase the statistical power to detect differences in each hypothesis test as in Figures D.10-D.12.

3.2. Simulation Results

For each simulation setting and run, we apply CAHC using a fixed number of nearest neighbors, set to 8, to define spatial links. Across all settings, CAHC consistently identified seven initial clusters, as determined by the spatially-informed silhouette score. Figure 2 compares this modified silhouette score with the standard version for a representative run. The results indicate that the modified silhouette score provides more reliable guidance for spatial clustering under CAHC.

As illustrated in Figure 3, CAHC detects the same seven clusters across all simulation settings. Thus, CAHC results in more clusters than the true number of clusters in the presence of RSP. To address this, we apply the repSpat framework to the CAHC output. Clusters are reassigned to a common label if they form a clique.

To evaluate the testing performance of repSpat, we conducted 100 simulation runs per setting and recorded two types of errors (1) false positives, where clusters sharing the same underlying distribution were identified as different; and (2) false negatives, where clusters with different distributions were incorrectly grouped as similar.

Table 2 reports the error rates across all simulation settings. Overall, repSpat demonstrates robust performance, maintaining low false discovery rates across

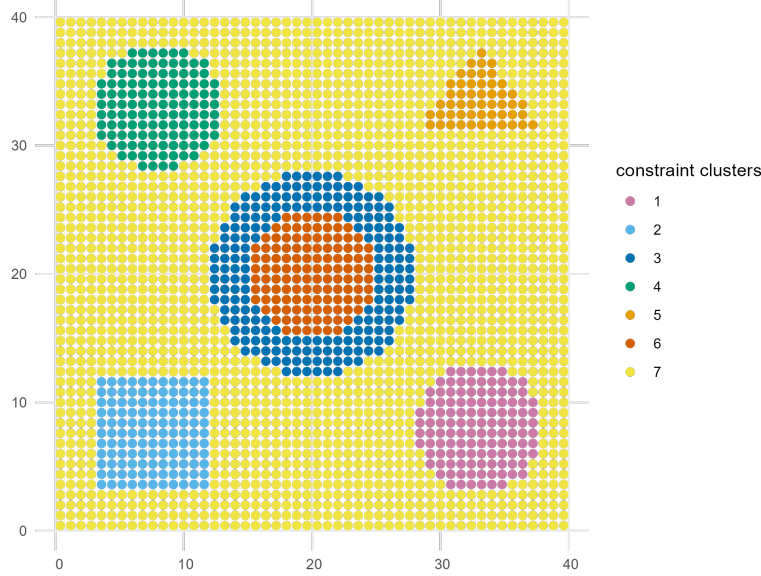


Figure 3: Constrained clustering result from CAHC for the simulation setting $n = 2500$, $p = 5$, and $\eta = 0.8$.

varying spatial autocorrelation strengths, dimensions, and number of locations. False negatives slightly increase under strong spatial autocorrelation ($\eta = 0.8$) and $p = 10$, possibly due to a suboptimal choice of the IMQ kernel parameter $c = 1$. However, such high autocorrelation levels are uncommon in most real-world spatial datasets. In practice, for the IMQ kernel, we can set the scale parameter c to the median or average of pairwise distances between samples. This choice increases the ability to detect dissimilarity, especially in moderate-to-high dimensions as discussed in Section 2.2.

To compute clustering accuracy, we use the adjusted Rand index (ARI), which quantifies the similarity between clustering results and the true class labels while correcting for chance agreement (Hubert and Arabie, 1985). ARI values range from 0 (no agreement beyond chance) to 1 (perfect concordance).

We evaluate the performance of repSpat and the recently proposed Banksy algorithm (Singhal et al., 2024). For Banksy, we use the same simulation setup, specifying an 8-nearest neighbor structure to generate spatial features and applying k -means clustering with $k = 3$. We use $\lambda = 0.8$, which encourages more weight on the spatial neighborhood information. Table 3 reports the median ARI across 100 simulation runs for each setting. Banksy results in ARI scores rang-

Table 2: Performance of repSpat over 100 simulation runs for each setting. A false positive occurs when a pair of spatially distant clusters sharing the same underlying distribution is identified as different. A false positive occurs when a pair of clusters with different distributions is incorrectly identified as similar.

n	p	ρ	False Negatives	False Positives
2500	5	0.3	0	0
	5	0.8	0.02	0
	10	0.3	0	0
	10	0.8	0.04	0
4900	5	0.3	0.01	0
	5	0.8	0	0
	10	0.3	0	0
	10	0.8	0	0

ing from 0.75 to 0.83, whereas repSpat consistently achieved a median ARI of 1 across all settings, indicating reliable recovery of RSP under varied spatial and distributional configurations

As shown in Figure 4(a), Banksy detects RSP but often misclassifies cluster boundaries, which reduces ARI performance. Banksy may improve performance if it is appropriately tuned for other clustering algorithms. However, this tuning may not be feasible in settings with many samples and irregularly shaped clusters. Figure 4(b) shows that the repSpat correctly identifies three clusters and the cluster boundaries. Using repSpat with features learned by Banksy may improve the detection of RSP. Although our simulations focused on continuous multivariate attributes, the repSpat framework naturally extends to other data types, such as binary or multinomial features, through the use of appropriate dissimilarity measures in the kernel, as demonstrated in the application.

These simulation results demonstrate that the repSpat framework is robust in identifying RSP across varying number of spatial points, multivariate attributes, and shapes.

Table 3: Median adjusted Rand index (ARI) for repSpat and Banksy over 100 simulation runs for each setting.

n	p	ρ	repSpat (ARI)	Banksy (ARI)
2500	5	0.3	1	0.81
	5	0.8	1	0.81
	10	0.3	1	0.82
	10	0.8	1	0.82
4900	5	0.3	1	0.75
	5	0.8	1	0.75
	10	0.3	1	0.83
	10	0.8	1	0.76

4. Real Data Application

We demonstrate repSpat to spatial proteomics data obtained through multiplexed ion beam imaging by time-of-flight (MIBI-TOF) technology from patients diagnosed with triple negative breast cancer (TNBC) (Keren et al., 2018). These TNBC tissue samples may contain multiple regions of similar spatial patterns that are mixtures of biomarkers. In particular, we focus on the repeated tumor microenvironments (TMEs).

The data set contains tissue samples from 41 patients, and each sample consists of spatial coordinates of cells within the tissue and expression levels for 36 protein markers. We use protein marker intensities and multivariate binary data derived from the marker threshold of these intensities (Bressan et al., 2023) to uncover TMEs in each tissue sample. Binary markers can be considered to remove noise and are expected to enhance clustering results. We apply repSpat with CAHC to all tissue samples, separately, and present the results of four patients. The remaining results are available in Appendix E. The four samples presented in this section exhibit diverse spatial patterns with varying cell counts. Figures 5(a) and 7(a) exhibit more spatially contiguous clustering patterns based on marker intensities compared to Figures 6(a) and 8(a). Among them, only Figure 5(a) displays a dense distribution of cell locations without large spatial gaps.

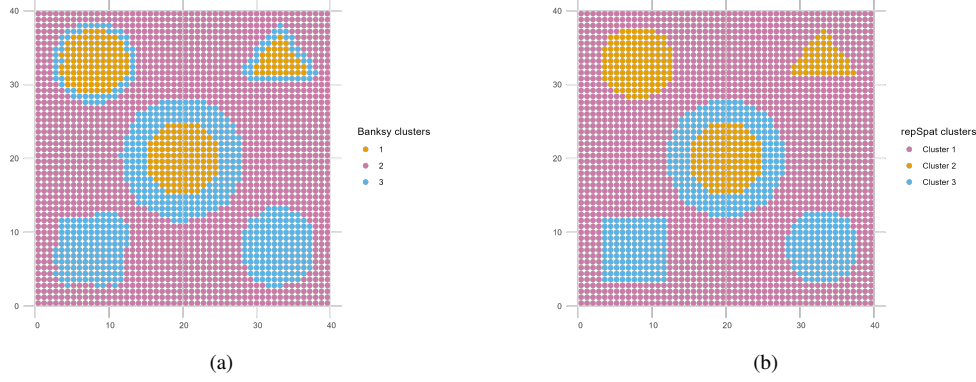


Figure 4: Example of (a) Banksy and (b) repSpat clustering results for the simulation setting with $n = 2500$, $p = 5$, and $\rho = 0.8$.

As the first step, we computed the Euclidean and Jaccard distance matrices for the marker intensities and binary markers, respectively. We applied CAHC with Ward linkage. Although Ward linkage typically favors compact, equally sized clusters, incorporating spatial constraints allows the detection of clusters with irregular shapes and varying sizes. We derived the spatial constraints using the k-nearest neighbor algorithm on the spatial coordinates of cells. In the second step, we varied the neighborhood size and the number of clusters based on the modified silhouette score to obtain the optimal CAHC clusters. Table 4 shows these two values for four selected samples based on marker intensities and binary markers. We observe that the number of clusters is the same using both data types. This might be because the spatial constraints are similar for both attributes, and the optimal clustering is based on the mean distance within and between clusters.

The results of the CAHC cluster with these optimal values are in Figures 5 - 8 (a) and (b) with marker intensities and binary markers, respectively. Figures 5 (a) and (b) show many small, well-separated clusters interspersed with larger regions, such as the dark blue and orange clusters, indicating a heterogeneous spatial pattern. In contrast, Figures 6 (a) and (b) contain fewer clusters, with the spatial domain dominated by three large, contiguous regions. Figures 7 (a) and (b) display a mixture of regional continuity and transitional zones, with the green cluster forming a curved structure. Figures 8 (a) and (b) present the most diffuse clustering, characterized by low spatial compactness, particularly evident in the widespread pink cluster.

Next, we applied repSpat to the CAHC clusters, followed by the cluster label reassignment step. As shown in Figures 5–8 (c) and (d), clustering based

Table 4: Optimal neighbourhood size and the number of clusters based on the modified silhouette score for the CAHC in four patient samples.

Samples	Marker intensities		Binary markers	
	Neighbourhood Size	Clusters	Neighbourhood Size	Clusters
04	8	7	8	7
05	8	4	8	4
26	6	7	6	7
39	8	5	6	5

on binary markers reveals more RSP. Thresholding the marker intensities reduces noise, enabling repSpat to identify repeated patterns more effectively across all tissue samples. In this analysis, we used the inverse multiquadratic (IMQ) kernel with $c = 1$, which provides stronger separation between distributions when paired with the Jaccard distance bounded within $[0, 1]$. This choice enhances the sensitivity of kernel to differences in distributions in the binary data setting.

In Figure 5 (e), the red cluster shares a similar spatial distribution with the blue clusters identified using binary markers in Figure 5 (f). These overlapping regions correspond to tumour cell populations based on cell type annotations (Keren et al., 2018). Similarly, in Figures 6-8 (f), the identified repeated clusters are predominantly enriched in mixed tumour cell populations, with relatively lower representation of immune cells.

5. Conclusion

We proposed a robust nonparametric framework for detecting repeated spatial patterns (RSP) in both geostatistical and lattice-based spatial processes. By integrating constrained agglomerative hierarchical clustering (CAHC) with a kernel-based maximum mean discrepancy (MMD) test and a block permutation procedure, repSpat addresses the common issue of over-segmentation in constrained clustering and enables the re-identification of spatially disjoint regions that share a similar distribution.

Our framework is nonparametric and supports a variety of attribute types through distance-based kernels. Simulation studies demonstrate that repSpat achieves high clustering accuracy in the presence of RSP while effectively controlling the

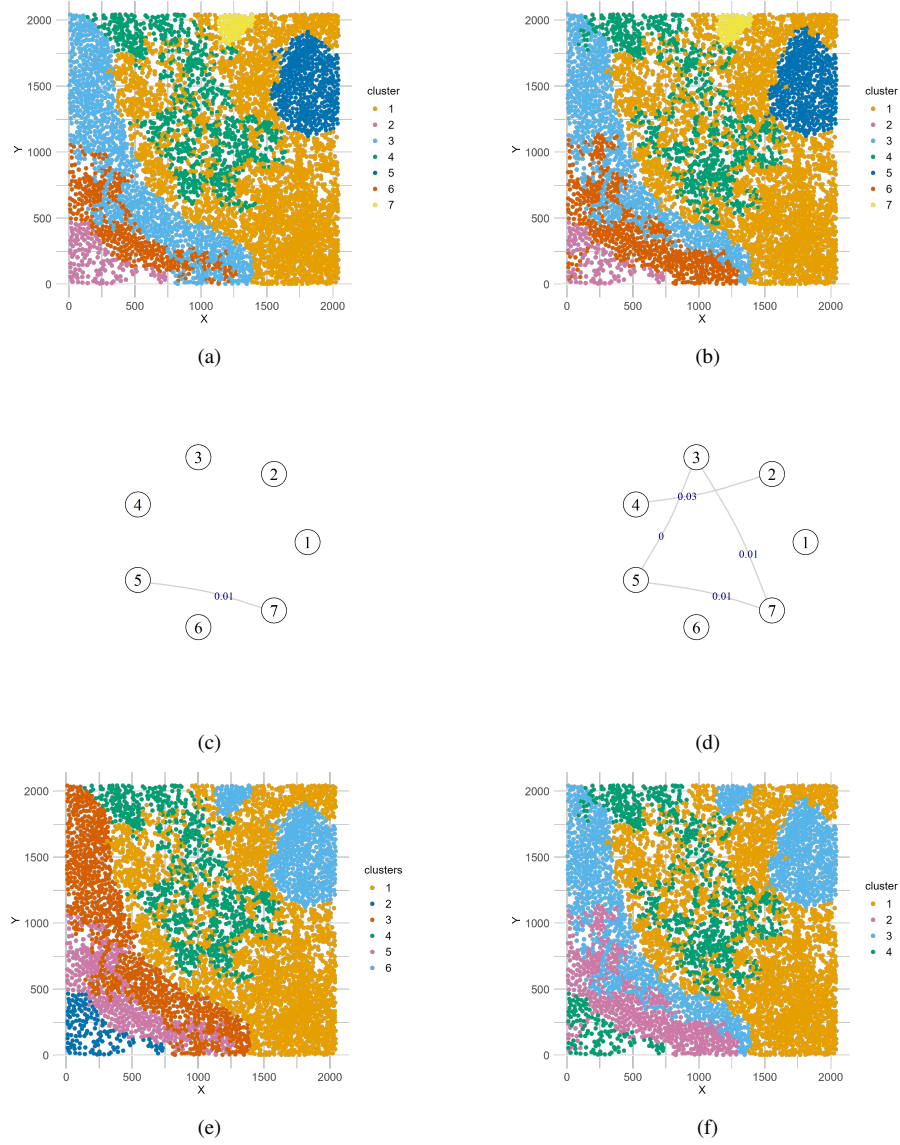


Figure 5: CAHC and repSpat results for Sample 04. CAHC clusters with (a) marker intensities and (b) binary markers. repSpat pairwise test results with (c) marker intensities and (d) binary markers. Reassigned cluster labels with (e) marker intensities and (f) binary markers.

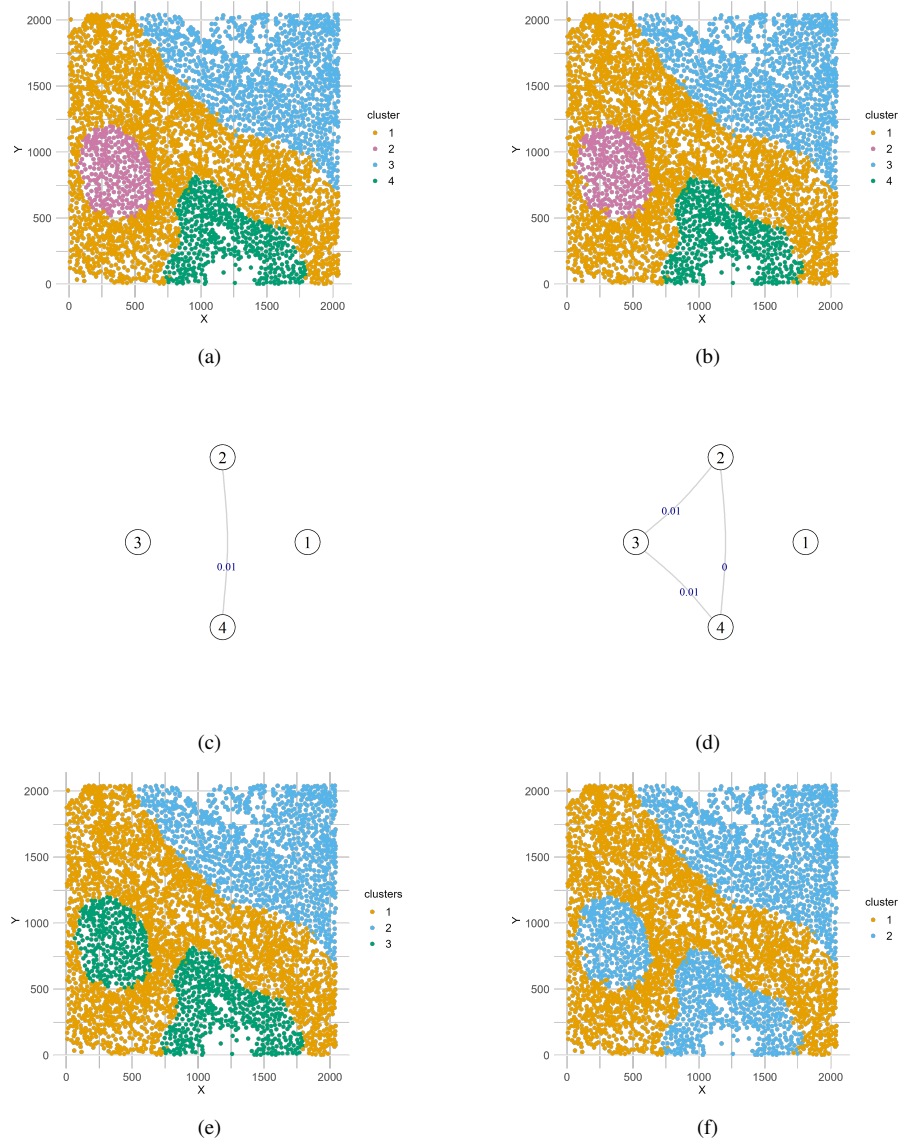


Figure 6: CAHC and repSpat results for Sample 05. CAHC clusters with (a) marker intensities and (b) binary markers. repSpat pairwise test results with (c) marker intensities and (d) binary markers. Reassigned cluster labels with (e) marker intensities and (f) binary markers.

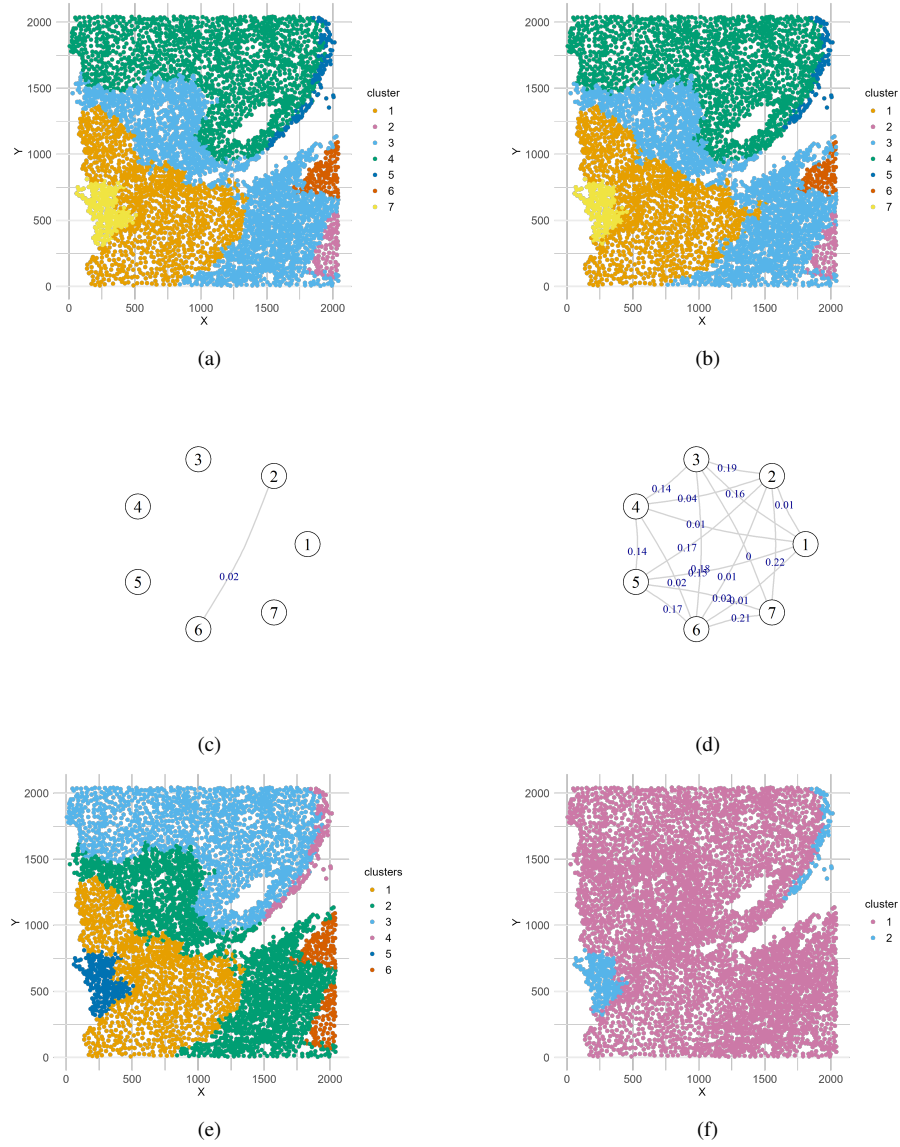


Figure 7: CAHC and repSpat results for Sample 26. CAHC clusters with (a) marker intensities and (b) binary markers. repSpat pairwise test results with (c) marker intensities and (d) binary markers. Reassigned cluster labels with (e) marker intensities and (f) binary markers.

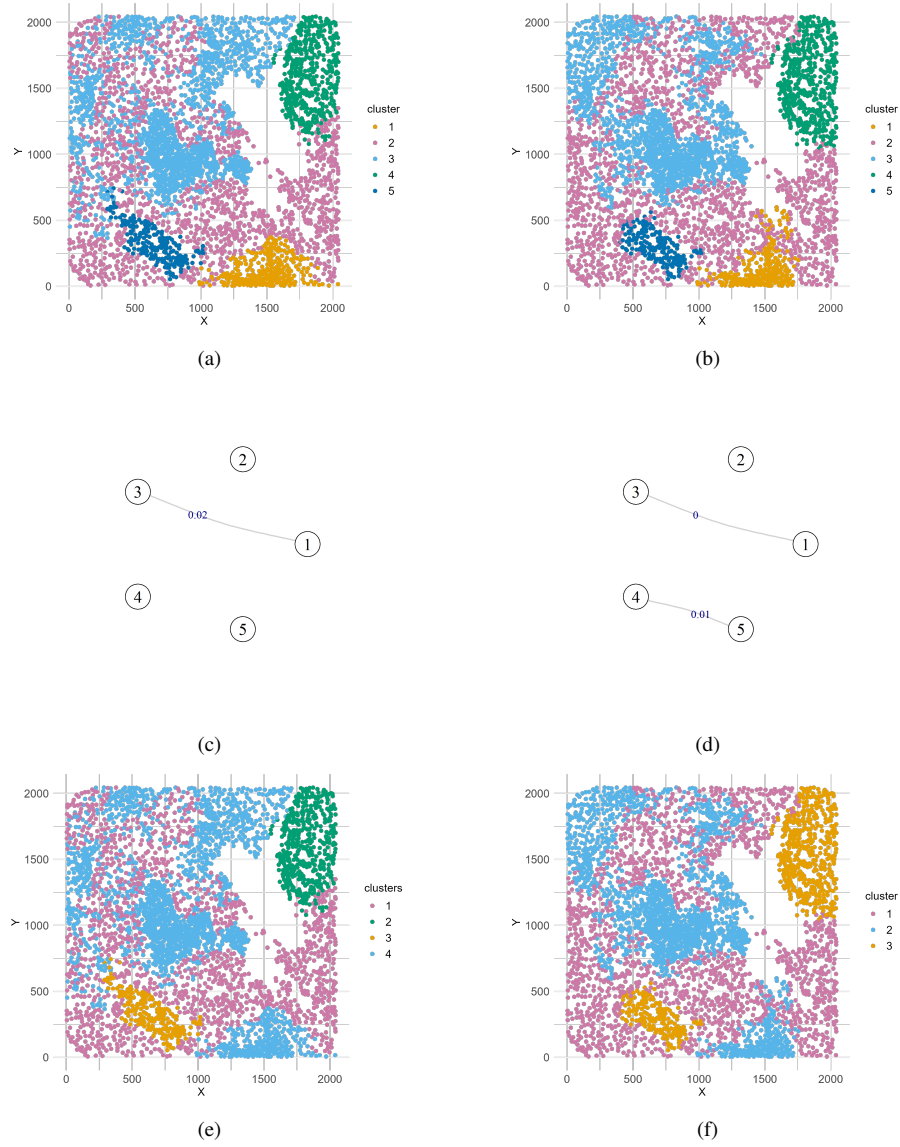


Figure 8: CAHC and repSpat results for Sample 39. CAHC clusters with (a) marker intensities and (b) binary markers. repSpat pairwise test results with (c) marker intensities and (d) binary markers. Reassigned cluster labels with (e) marker intensities and (f) binary markers.

false discovery rate under weak to moderate spatial dependence. When applied to spatial proteomics data, repSpat successfully uncovers repeated patterns, highlighting its utility for real-world applications, particularly in the spatial omics domain.

While repSpat is effective in detecting repeated patterns, it exhibits limited sensitivity to slight changes in spatial dependence alone, such as variations in autocorrelation strength. This points to an opportunity for future research to explore dependence-sensitive kernels or strategies for selecting kernel parameters.

In future work, we aim to extend this framework to: (1) incorporate other types of constrained clustering algorithms followed by repSpat; (2) perform variable selection to enhance clustering interpretability and power in detecting dissimilarity between cluster distribution; and (3) develop Bayesian models that provide uncertainty quantification for cluster assignments.

Although this study focused on Gaussian and binary attributes, the proposed methodology is readily extensible to other data types such as compositional or count-valued observations through suitable dissimilarity measures and kernel functions. Given its robustness across different sample sizes, attribute dimensions, and spatial dependence levels, repSpat offers a flexible and general-purpose framework for discovering repeated spatial patterns in complex spatial datasets.

Funding

This work was supported by the Natural Sciences and Engineering Research Council of Canada (NSERC) through the Discovery Grant [RGPIN-2022-05272] and Discovery Launch Supplement [DGECR-2022-00465].

Acknowledgement

Partial support for computational resources was provided by SHARCNET (www.sharcnet.ca) and the Digital Research Alliance of Canada (www.alliancecan.ca). Jamie D. McNicol (Department of Medicine, McMaster Immunology Research Center, Hamilton, Ontario, Canada) provided us with guidance on accessing the dataset and the threshold for protein markers used in the application.

Appendix A. Block Permutation Steps

1. Create attribute-based blocks within $C^{(g)}$ and $C^{(h)}$ using k-Means clustering. The number of blocks $b^{(g)}$ and $b^{(h)}$ for each cluster is determined based on the optimal neighborhood size m and the number of observations $n^{(g)}$ and $n^{(h)}$ in each cluster from the CAHC:

$$\text{Number of blocks} = \frac{\text{Number of observations in the cluster}}{\text{Neighborhood size}}. \quad (\text{A.1})$$

If the neighborhood size exceeds the number of observations in a cluster, we assign a single block.

2. Randomly select blocks from both clusters without replacement until the number of observations in the selected blocks exceeds the size of the smaller cluster (assume $C^{(g)}$).
3. Assign the selected blocks to $C^{(g)}$, and assign the remaining blocks to $C^{(h)}$.

Appendix B. Example for Reassigning Cluster Labels

Figure B.9 illustrates a graph constructed from pairwise test results among eight clusters. Two distinct fully connected subgraphs emerge: one comprising nodes 1, 3, and 4, and another comprising nodes 2, 5, 6, 7, and 8. Based on the merging rule, we combine clusters 1, 3, and 4 into one cluster, and clusters 2, 5, 6, 7, and 8 into another. Notably, the edge between nodes 1 and 5 is excluded from this decision, as its associated $\text{MMD}_{\text{obs}}^2$ value is considerably larger than those within the subgraphs.

Appendix C. Asymptotic Properties of MMD^2 under Second-Order Stationarity

We define the biased version of MMD^2 to test differences in the distribution of $X(s)$ between pairs of clusters obtained from constrained agglomerative hierarchical clustering (CAHC).

Recall that $C^{(g)} = \{s_1^{(g)}, \dots, s_{n_g}^{(g)}\}$ and $C^{(h)} = \{s_1^{(h)}, \dots, s_{n_h}^{(h)}\}$ denote two such clusters, each corresponding to a spatial subregion. The associated multivariate attributes are given by $X^{(g)} = \{X(s_i^{(g)}) \in \mathbb{R}^p : i = 1, \dots, n_g\}$ and $X^{(h)} = \{X(s_j^{(h)}) \in \mathbb{R}^p : j = 1, \dots, n_h\}$.

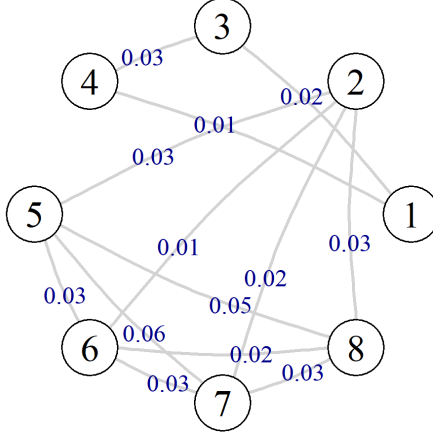


Figure B.9: Graph constructed from pairwise MMD^2 tests across 8 clusters. Edges represent not enough evidence to find differences, with edge weights corresponding to $\text{MMD}_{\text{obs}}^2$ values.

We assume that all clusters $\mathcal{C}^{(g)}$ and $\mathcal{C}^{(h)}$ are disjoint, and $\mathbf{X}^{(g)}$ and $\mathbf{X}^{(h)}$ are second-order stationary.

Recall that $k : \mathcal{X} \times \mathcal{X} \rightarrow \mathbb{R}$ is a positive definite kernel, where $\mathcal{X} \subseteq \mathbb{R}^p$. Note that k is a Lipschitz function. Moreover, the RKHS inner product satisfies $\langle f, k(\cdot, \mathbf{x}) \rangle_{\mathcal{H}_k} = f(\mathbf{x})$. This also implies that for any $\mathbf{x}, \mathbf{y} \in \mathcal{X}$, we have $k(\mathbf{x}, \mathbf{y}) = \langle k(\cdot, \mathbf{x}), k(\cdot, \mathbf{y}) \rangle_{\mathcal{H}_k}$.

We now define the unbiased version of MMD^2 following (Gretton et al., 2012), where i and j are spatial indices:

$$\begin{aligned} \widehat{\text{MMD}}^2(\mathbf{X}^{(g)}, \mathbf{X}^{(h)}; \mathcal{H}_k) &= \frac{1}{n_g(n_g - 1)} \sum_{\substack{i,j=1 \\ i \neq j}}^{n_g} k(\mathbf{x}_i^{(g)}, \mathbf{x}_j^{(g)}) + \frac{1}{n_h(n_h - 1)} \sum_{\substack{i,j=1 \\ i \neq j}}^{n_h} k(\mathbf{x}_i^{(h)}, \mathbf{x}_j^{(h)}) \\ &\quad - \frac{2}{n_g n_h} \sum_{i=1}^{n_g} \sum_{j=1}^{n_h} k(\mathbf{x}_i^{(g)}, \mathbf{x}_j^{(h)}). \end{aligned} \quad (\text{C.1})$$

Following the asymptotics of U-statistics in chapter 12 of Van der Vaart (2000), the formulation of MMD^2 as a U-statistic in Gretton et al. (2012), the definition of covariance operators in \mathcal{H}_k from Chérif-Abdellatif and Alquier (2022), and the spatial mixing conditions from Sherman (1996), we show that the biased MMD^2 in (C.1) is asymptotically consistent.

Assume $n_g = n_h = N$. Then, (C.1) becomes a one-sample U-statistic of order two as in Gretton et al. (2012). When $n_g \neq n_h$, MMD^2 becomes a von Mises functional, but under the same regularity conditions, it also remains consistent.

Let $z_i = (x_i^{(g)}, x_i^{(h)})^\top$ and $z_j = (x_j^{(g)}, x_j^{(h)})^\top$ denote samples of bivariate vectors. Define

$$h(z_i, z_j) = k(x_i^{(g)}, x_j^{(g)}) + k(x_i^{(h)}, x_j^{(h)}) - k(x_i^{(g)}, x_j^{(h)}) - k(x_j^{(g)}, x_i^{(h)}).$$

Then,

$$\text{MMD}_N^2 = \frac{1}{N(N-1)} \sum_{i \neq j} h(z_i, z_j).$$

Given MMD_N^2 is unbiased, we now show that $\mathbb{E}[(\text{MMD}_N^2)^2] < \infty$. Following the proof of theorem 12.3 in Van der Vaart (2000), we have:

$$\mathbb{E}[(\text{MMD}_N^2)^2] \leq \frac{1}{N(N-1)} \sum_{i \neq j} \sum_{u \neq v} \text{Cov}(h(z_i, z_j), h(z_u, z_v)). \quad (\text{C.2})$$

The covariance $\text{Cov}(h(z_i, z_j), h(z_u, z_v))$ depends on the spatial lags $|s_i - s_u|$ and $|s_j - s_v|$ for $s_i, s_u \in C^{(g)}$ and $s_j, s_v \in C^{(h)}$. The covariance is defined over the RKHS \mathcal{H}_k . Following Definition 2.1 in Chérif-Abdellatif and Alquier (2022), we define the spatial dependence coefficient via the kernel mean embedding:

$$Q_\ell = \left| \mathbb{E} \langle k(x_s, \cdot) - \mu_P, k(x_{s+\ell}, \cdot) - \mu_P \rangle_{\mathcal{H}_k} \right|, \quad (\text{C.3})$$

where $\mu_P := \mathbb{E}_{\mathbf{X} \sim P}[k(\cdot, \mathbf{x})]$. Since $C^{(g)}$ and $C^{(h)}$ are disjoint, the spatial lags in their respective domains are distinct. Therefore, for the collection of spatial lags \mathcal{L} over either process $\mathbf{X}^{(g)}$ or $\mathbf{X}^{(h)}$, we can show that $\sum_{\ell \in \mathcal{L}} Q_\ell < \infty$.

Suppose we focus on cluster $C^{(g)}$. Following Sherman (1996), define a mixing coefficient:

$$\alpha_\kappa(\ell) := \sup \{ \mathbb{P}(AB) - \mathbb{P}(A)\mathbb{P}(B) : A \in \mathcal{F}(\Delta_1), B \in \mathcal{F}(\Delta_2), \\ |\Delta_1| \leq \kappa, |\Delta_2| \leq \kappa, d(\Delta_1, \Delta_2) \geq \ell \}, \quad (\text{C.4})$$

where $\Delta_j \subset C^{(g)}$, $\mathcal{F}(\Delta_j)$ is the σ -field generated by $\{X^{(g)}(s_i) : i \in \Delta_j\}$, and $d(A, B) = \inf\{|s_i - s_j| : s_i \in A, s_j \in B\}$.

Following Sherman (1996), $\alpha_\kappa(\ell)$ is a model-free mixing coefficient. We will show that $\sup\{\alpha_\kappa(\ell)/\kappa\} \rightarrow 0$ as $\kappa \rightarrow \infty$ or as spatial lag ℓ increases.

Let m denote the optimal spatial neighborhood size used in CAHC. Then there exists $\ell_o < \infty$ such that $\alpha_\kappa(\ell_o)$ is negligible. This lag can be approximated by n_g/m , where n_g is the size of cluster $C^{(g)}$. Following Bolthausen (1982), if $\alpha_\kappa(\ell)/\kappa \rightarrow 0$ and $C^{(g)}$ is compact, then $\rho(\ell)$, the spatial dependence at lag ℓ , decays as $\ell \rightarrow \ell_o$.

Under this mixing condition, we now show that $\sum_{\ell \in \mathcal{L}} Q_\ell < K \cdot \sum_{\ell \in \mathcal{L}} \rho(\ell)$

$$\begin{aligned} Q_\ell &= \mathbb{E} \left| \langle k(x_s, \cdot) - \mu_P, k(x_{s+\ell}, \cdot) - \mu_P \rangle_{\mathcal{H}_k} \right| \\ &= \mathbb{E} \left| \langle k(x_s, \cdot), k(x_{s+\ell}, \cdot) \rangle_{\mathcal{H}_k} - \langle k(x_s, \cdot), \mu_P \rangle_{\mathcal{H}_k} - \langle \mu_P, k(x_{s+\ell}, \cdot) \rangle_{\mathcal{H}_k} + \langle \mu_P, \mu_P \rangle_{\mathcal{H}_k} \right| \\ &\leq \mathbb{E} \left| \langle k(x_s, \cdot), k(x_{s+\ell}, \cdot) \rangle_{\mathcal{H}_k} \right| + \mathbb{E} \left| \langle k(x_s, \cdot), \mu_P \rangle_{\mathcal{H}_k} \right| + \\ &\quad \mathbb{E} \left| \langle \mu_P, k(x_{s+\ell}, \cdot) \rangle_{\mathcal{H}_k} \right| + \mathbb{E} \left| \langle \mu_P, \mu_P \rangle_{\mathcal{H}_k} \right| \\ &\leq \mathbb{E} \left| \langle k(x_s, \cdot), k(x_{s+\ell}, \cdot) \rangle_{\mathcal{H}_k} \right| \end{aligned} \tag{C.5}$$

$$\leq K \cdot \mathbb{E} \|x_s - x_{s+\ell}\| \tag{C.6}$$

$$\tag{C.7}$$

Equation (C.5) holds because the terms involving μ_P are constants, and thus the sum of expectations is bounded independently of lag ℓ . Therefore, for bounding the decay in spatial dependence with ℓ , the dominant term is the expectation of the inner product $k(x_s, \cdot)$ and $k(x_{s+\ell}, \cdot)$. Since k is Lipschitz and bounded, there exists K such that (C.6) holds and decays with $\rho(\ell)$.

Finally, by theorem 1 in Sen (1972), $\sqrt{N}(\text{MMD}_N^2 - \text{MMD}^2) \xrightarrow{P} 0$. Thus, under second-order stationarity and model-free mixing conditions, the MMD_N^2 statistic is asymptotically consistent.

Appendix D. Sampling distribution of MMD^2 Using Monte Carlo Method

We conducted simulations by varying the number of spatial points n , attribute dimension p , spatial autocorrelation η , kernel type, and kernel-specific parameters c to investigate the sampling distribution of the MMD^2 statistic under scenarios where the underlying distributions of two clusters are either identical or different. Notably, we found that the inverse multiquadratic (IMQ) kernel with shape parameter $c \geq 1$ shifts the distribution of MMD^2 further away from zero when the cluster distributions differ, thereby enhancing sensitivity. The IMQ kernel also

increases the range of MMD^2 values under the alternative hypothesis, improving the ability to detect differences in distributions.

Appendix D.1. Sampling Distribution of MMD^2 Under Differences in Mean Function, μ

As described in in Section 3.1, we simulate random fields for patches in two regions with a varying means $\mu_1 = 4$, $\mu_2 = 10$ and variance $\tau^2 = 1$, and the same covariance function with spatial autocorrelation $\eta = 0.3$ or $\eta = 0.8$. We approximate the sampling distribution of MMD^2 for each setting using the Monte Carlo method.

We demonstrate that the IMQ kernel with parameter $c \geq 1$ exhibits the greatest statistical power in detecting differences between the underlying distributions of clusters that are spatially separated.

Appendix D.2. Sampling distribution of MMD^2 under differences in spatial covariance (controlled by η)

We simulate spatial random fields over patches in two regions, each with a constant mean $\mu = 10$ and marginal variance $\tau^2 = 1$. To introduce differences in distributions, we vary the spatial autocorrelation parameters: $\eta_1 = 0.3$ for one region and $\eta_2 = 0.8$ for the other.

Although differences in spatial autocorrelation affect the covariance structure of the underlying spatial distributions, the MMD^2 statistic exhibits limited sensitivity to such differences in this setting. This is because the marginal distributions remain nearly identical and the shift in spatial dependence is relatively subtle in a conditional autoregressive model, making it difficult for MMD^2 to detect distributional differences that are driven solely by changes in spatial autocorrelation.

Appendix E. Supplementary Materials

The following are the supplementary materials related to this article.

1. Simulation workflow to produce the figures and tables in Section 3.
 - See `AppD-supplementary-materials-simulation-study.pdf` for details.
 - See `AppD-simulation-setup-and-silhouette-scores.pdf` for selecting the number of clusters using the modified silhouette score for one simulation run in the `repSpat` framework.

2. The workflow for applying the repSpat method to MIBI-TOF TNBC protein intensities data Keren et al. (2018) described in Section 4.
 - See AppD-repSpat-MIBI-TOF-TNBC-intensities-10-samples.pdf for details.
3. The workflow for applying the repSpat method to MIBI-TOF TNBC binary data Keren et al. (2018) described in Section 4.
 - See AppD-repSpat-MIBI-TOF-TNBC-binary-10-samples.pdf for details.
4. R functions for repSpat
 - The development version of the R package repSpat is available in a GitHub repository and is available upon request.
5. Simulation workflow for sampling distribution of MMD²
 - See AppD-MMD-sampling-distribution-sim-data for simulating data.
 - See AppD-MMD-sampling-distribution-Monte-Carlo for creating Figures D.10 - D.17

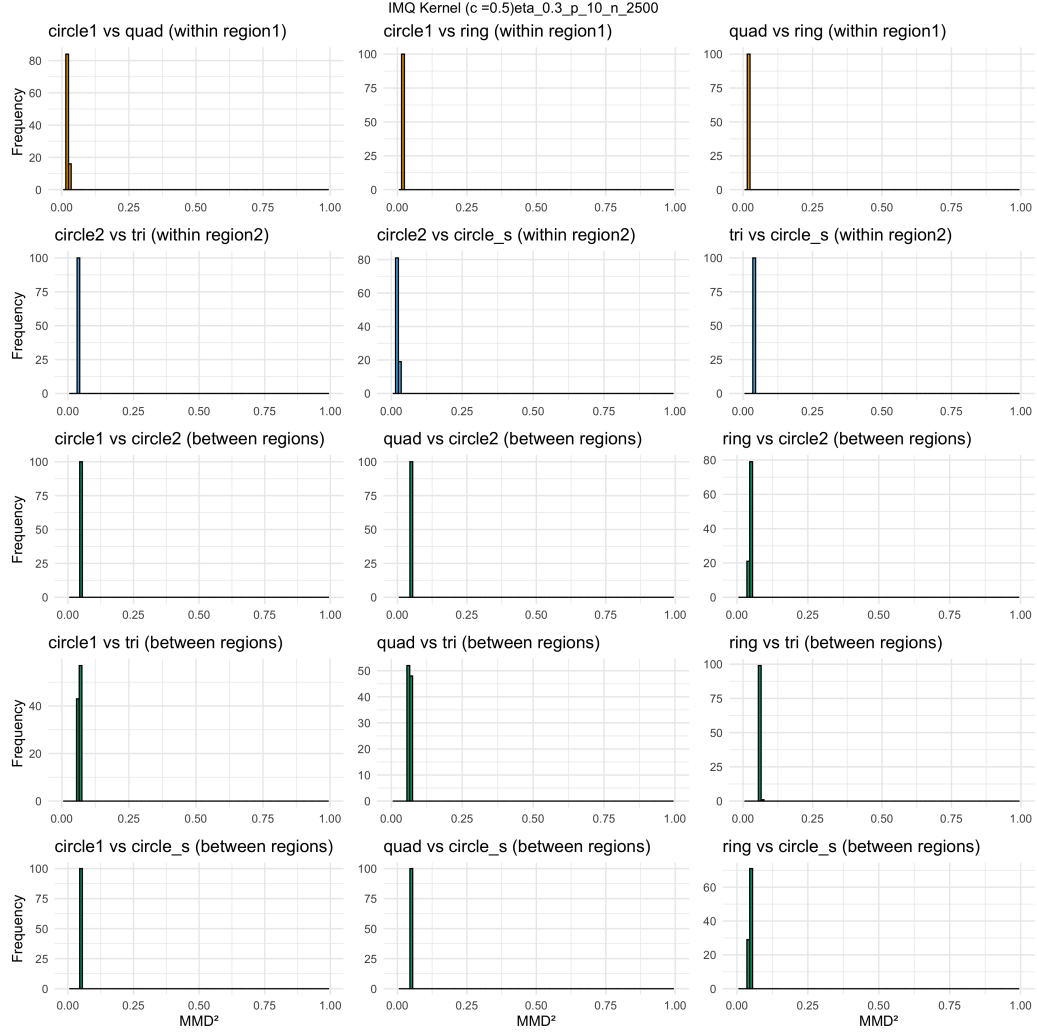


Figure D.10: Sampling distribution of MMD^2 using the IMQ kernel with $c = 0.5$, spatial autocorrelation $\eta = 0.3$, number of attributes $p = 10$, and $n = 2500$. Rows 1–2: comparisons between clusters from regions simulated under the same distribution. Rows 3–5: comparisons between clusters from regions simulated under different distributions.

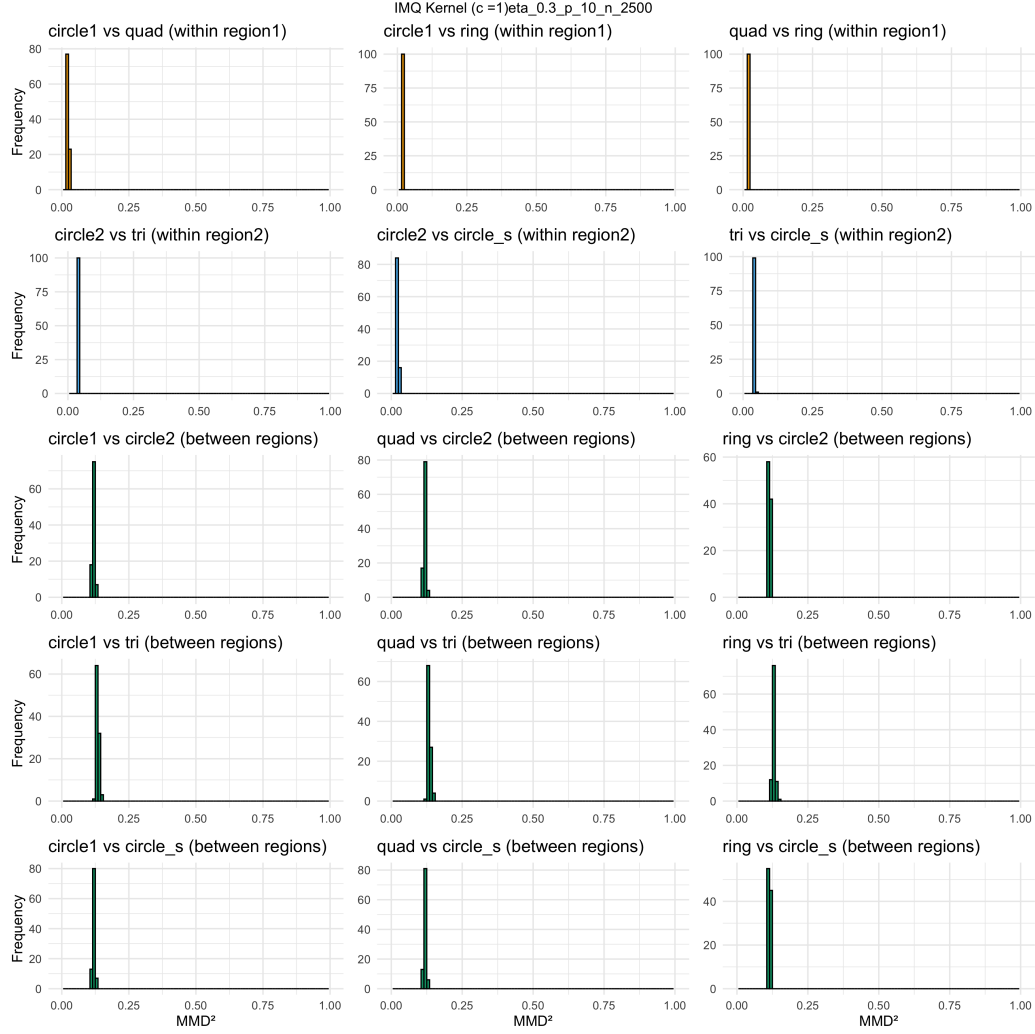


Figure D.11: Sampling distribution of MMD^2 using the IMQ kernel with $c = 1$, spatial autocorrelation $\eta = 0.3$, number of attributes $p = 10$, and $n = 2500$. Rows 1–2: comparisons between clusters from regions simulated under the same distribution. Rows 3–5: comparisons between clusters from regions simulated under different distributions.

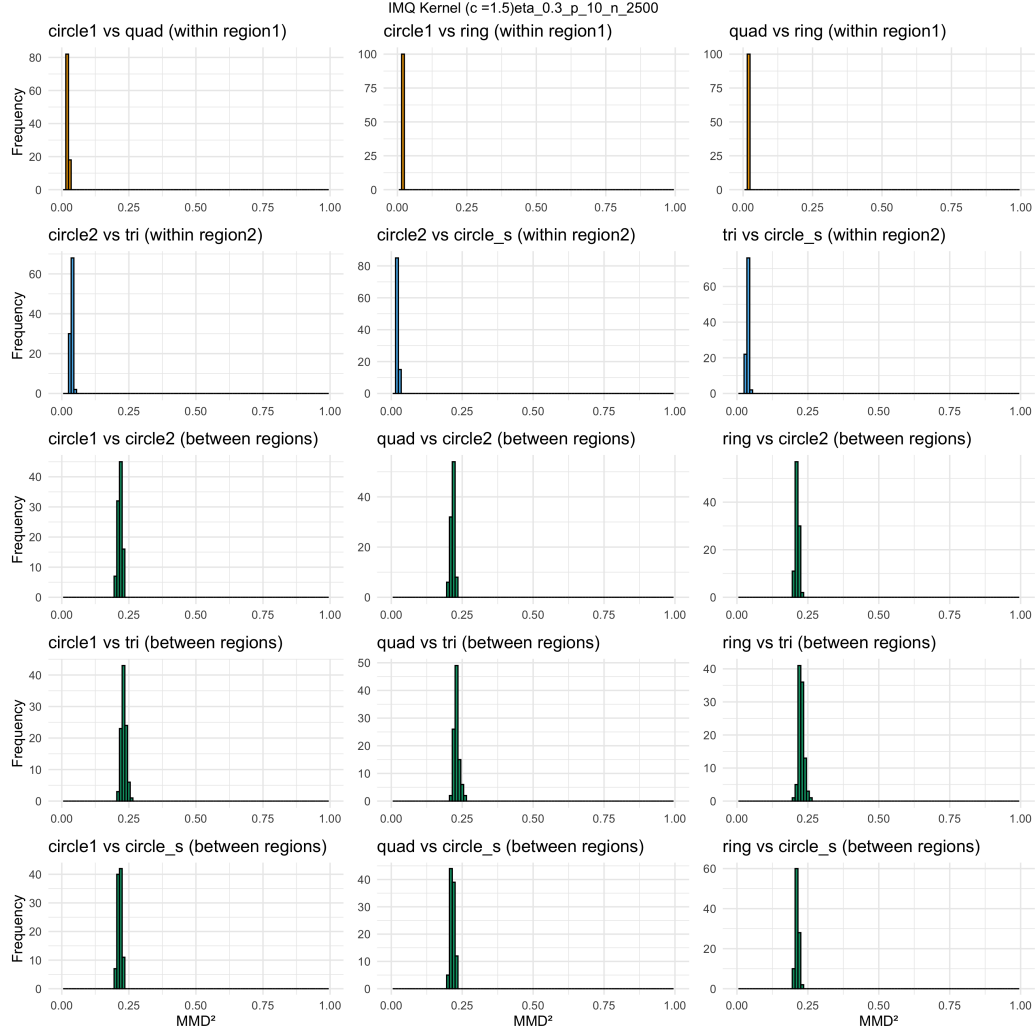


Figure D.12: Sampling distribution of MMD^2 using the IMQ kernel with $c = 1.5$, spatial autocorrelation $\eta = 0.3$, number of attributes $p = 10$, and $n = 2500$. Rows 1–2: comparisons between clusters from regions simulated under the same distribution. Rows 3–5: comparisons between clusters from regions simulated under different distributions.

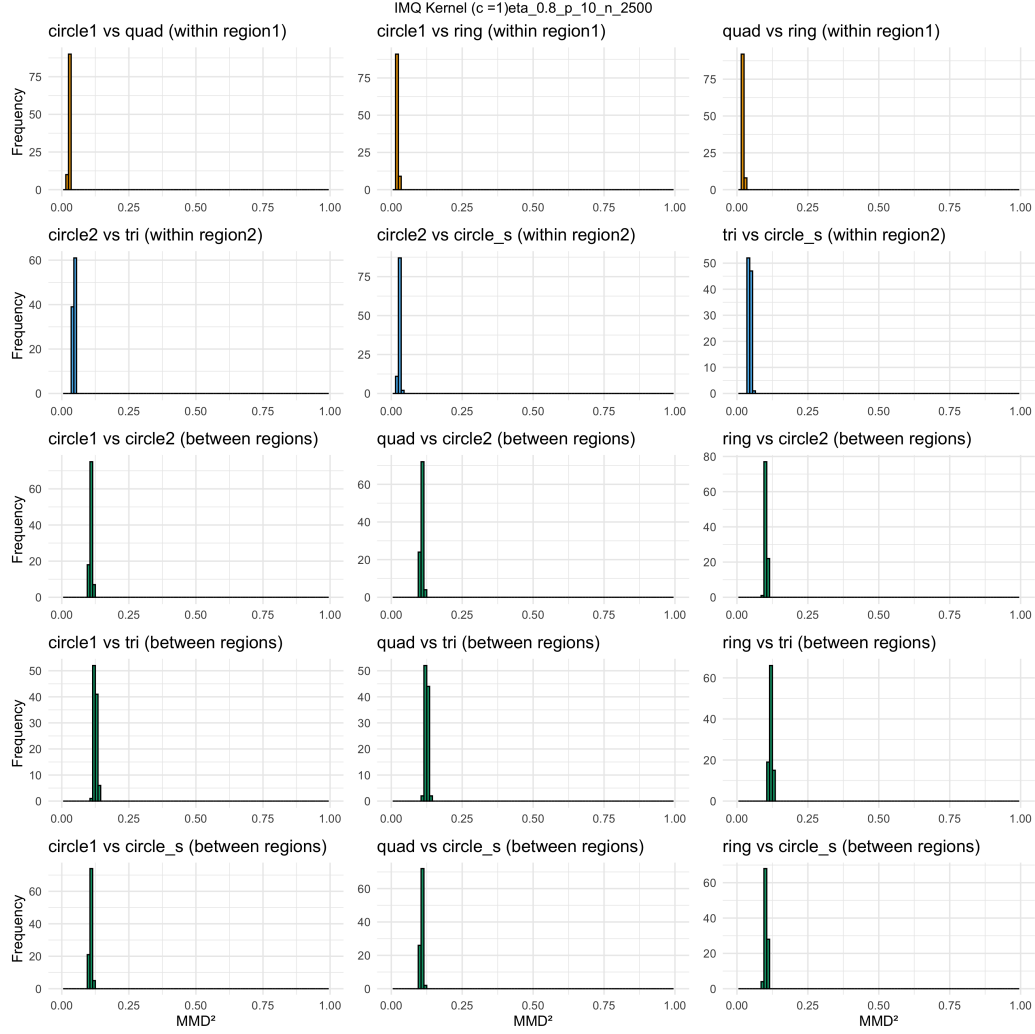


Figure D.13: Sampling distribution of MMD^2 using the IMQ kernel with $c = 1$, spatial autocorrelation $\eta = 0.8$, number of attributes $p = 10$, and $n = 2500$. Rows 1–2: comparisons between clusters from regions simulated under the same distribution. Rows 3–5: comparisons between clusters from regions simulated under different distributions.

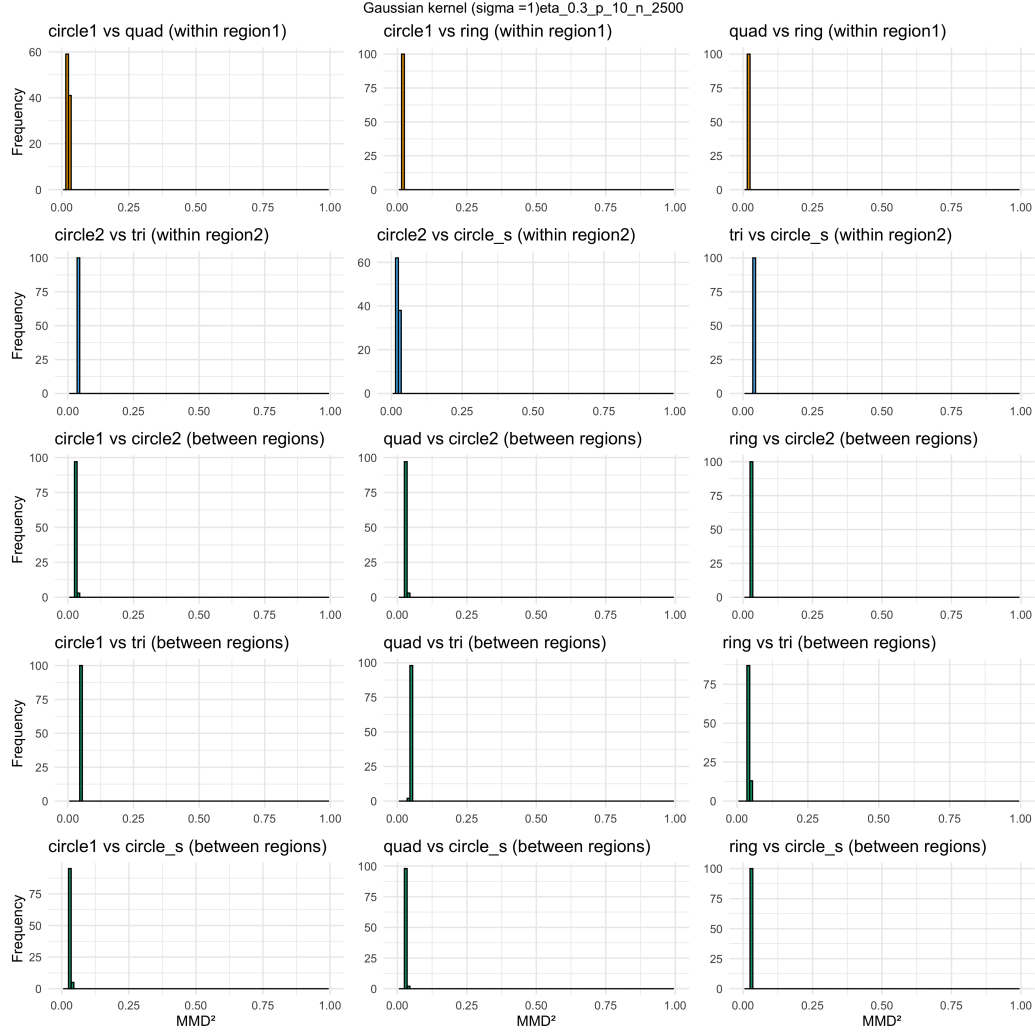


Figure D.14: Sampling distribution of MMD^2 using the Gaussian kernel with $\sigma = 1$, spatial autocorrelation $\eta = 0.3$, number of attributes $p = 10$, and $n = 2500$. Rows 1–2: comparisons between clusters from regions simulated under the same distribution. Rows 3–5: comparisons between clusters from regions simulated under different distributions.

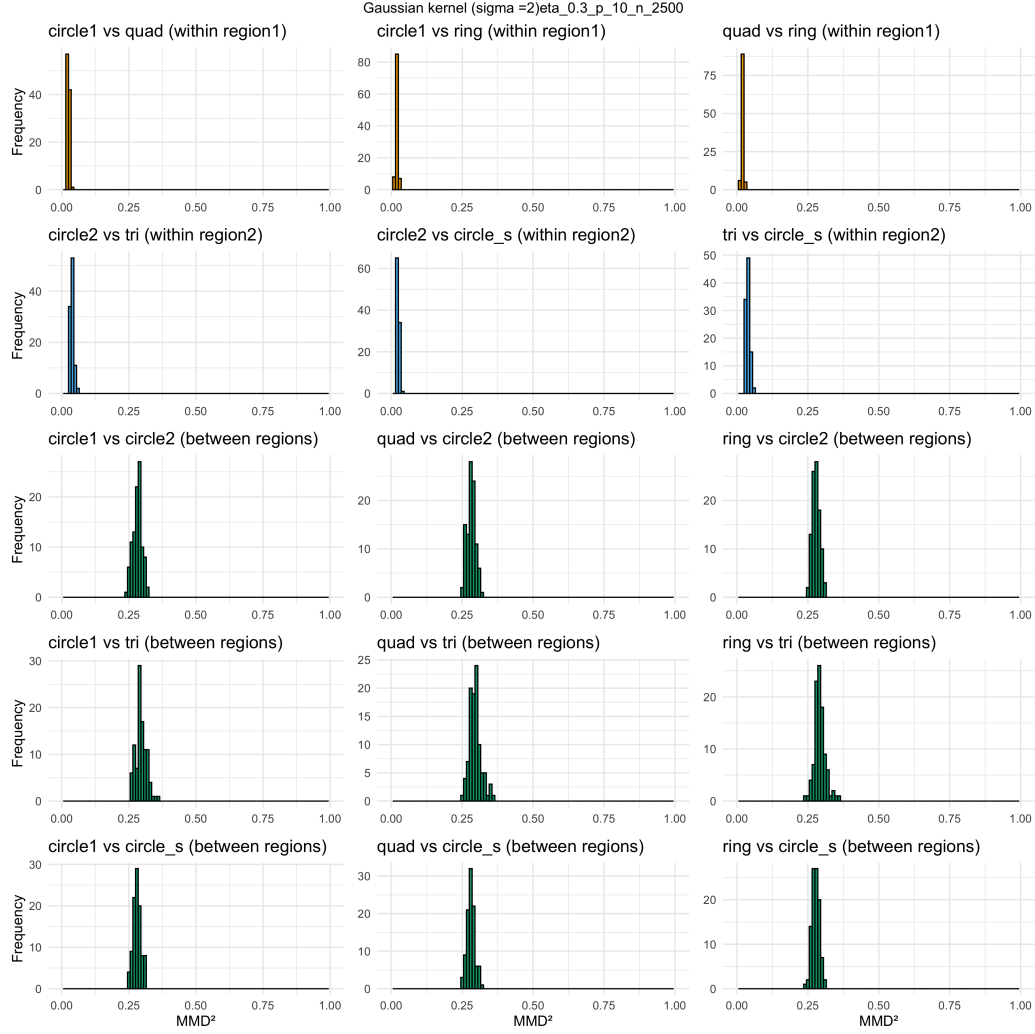


Figure D.15: Sampling distribution of MMD^2 using the Gaussian kernel with $\sigma = 2$, spatial autocorrelation $\eta = 0.3$, number of attributes $p = 10$, and $n = 2500$. Rows 1–2: comparisons between clusters from regions simulated under the same distribution. Rows 3–5: comparisons between clusters from regions simulated under different distributions.

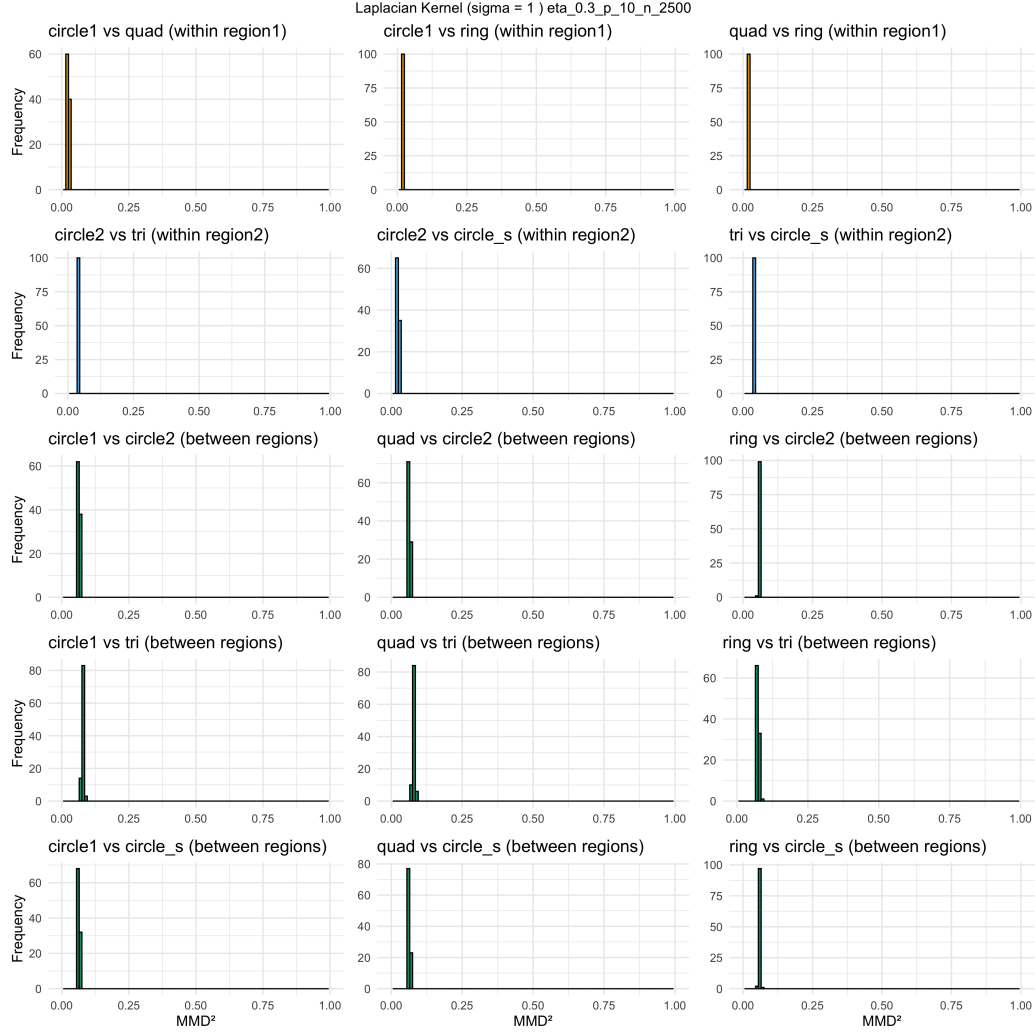


Figure D.16: Sampling distribution of MMD^2 using the Laplacian kernel with $\sigma = 1$, spatial autocorrelation $\eta = 0.3$, number of attributes $p = 10$, and $n = 2500$. Rows 1–2: comparisons between clusters from regions simulated under the same distribution. Rows 3–5: comparisons between clusters from regions simulated under different distributions.

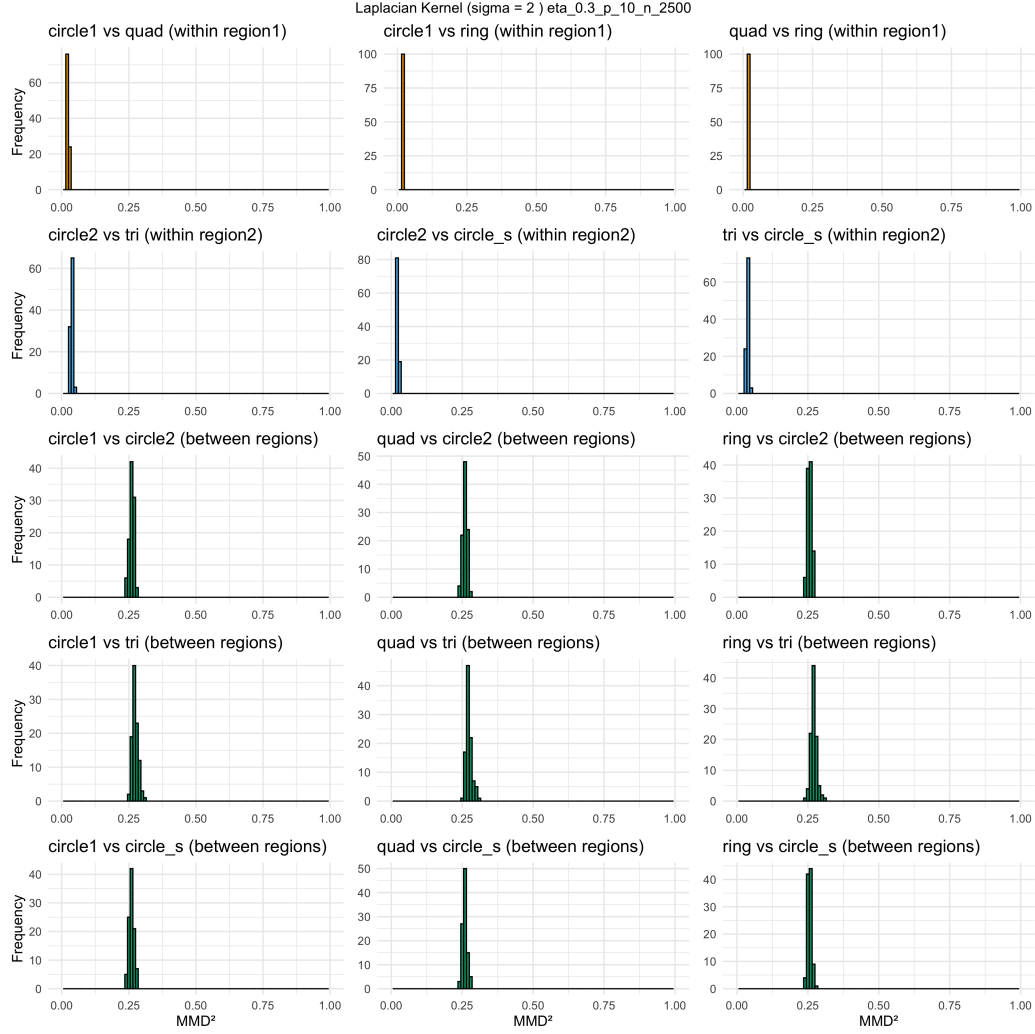


Figure D.17: Sampling distribution of MMD^2 using the Laplacian kernel with $\sigma = 2$, spatial autocorrelation $\eta = 0.3$, number of attributes $p = 10$, and $n = 2500$. Rows 1–2: comparisons between clusters from regions simulated under the same distribution. Rows 3–5: comparisons between clusters from regions simulated under different distributions.

References

- Abolhassani, A., Prates, M.O., 2021. An up-to-date review of scan statistics. *Statistic Surveys* 15, 111–153.
- Benevento, A., Durante, F., 2024. Correlation-based hierarchical clustering of time series with spatial constraints. *Spatial Statistics* 59, 100797.
- Benjamini, Y., Hochberg, Y., 1995. Controlling the false discovery rate: a practical and powerful approach to multiple testing. *Journal of the Royal statistical society: series B (Methodological)* 57, 289–300.
- Berlinet, A., Thomas-Agnan, C., 2011. Reproducing kernel Hilbert spaces in probability and statistics. Springer Science & Business Media.
- Besag, J., 1974. Spatial interaction and the statistical analysis of lattice systems. *Journal of the Royal Statistical Society: Series B (Methodological)* 36, 192–225.
- Bolthausen, E., 1982. On the central limit theorem for stationary mixing random fields. *The Annals of Probability* , 1047–1050.
- Bressan, D., Battistoni, G., Hannon, G.J., 2023. The dawn of spatial omics. *Science (New York, N.Y.)* 381, eabq4964. doi:10.1126/science.abq4964.
- de Bruijn, I., Nikolov, M., Lau, C., Clayton, A., Gibbs, D.L., Mittraka, E., Pozhdayeva, D., Lash, A., Sumer, S.O., Altreuter, J., et al., 2025. Sharing data from the human tumor atlas network through standards, infrastructure and community engagement. *Nature Methods* , 1–8.
- Chérif-Abdellatif, B.E., Alquier, P., 2022. Finite sample properties of parametric MMD estimation: Robustness to misspecification and dependence. *Bernoulli* 28, 181–213. doi:10.3150/21-BEJ1338.
- Dries, R., Zhu, Q., Dong, R., Eng, C.H.L., Li, H., Liu, K., Fu, Y., Zhao, T., Sarkar, A., Bao, F., George, R.E., Pierson, N., Cai, L., Yuan, G.C., 2021. Giotto: a toolbox for integrative analysis and visualization of spatial expression data. *Genome Biology* 22, 78. doi:10.1186/s13059-021-02286-2.
- Editorial Board, 2024. Method of the year 2024: spatial proteomics. *Nature Methods* 21, 2195–2196. doi:10.1038/s41592-024-02565-3. editorial.

- Ester, M., Kriegel, H.P., Sander, J., Xu, X., 1996. A density-based algorithm for discovering clusters in large spatial databases with noise, in: *Proceedings of the Second International Conference on Knowledge Discovery and Data Mining*, AAAI Press, Portland, Oregon. pp. 226–231.
- Gretton, A., Borgwardt, K., Rasch, M., Schölkopf, B., Smola, A., 2006. A kernel method for the two-sample-problem. *Advances in neural information processing systems* 19.
- Gretton, A., Borgwardt, K.M., Rasch, M.J., Schölkopf, B., Smola, A., 2012. A kernel two-sample test. *The Journal of Machine Learning Research* 13, 723–773.
- Guillot, G., Rousset, F., 2013. Dismantling the mantel tests. *Methods in ecology and evolution* 4, 336–344.
- Guénard, G., Legendre, P., 2022. Hierarchical Clustering with Contiguity Constraint in R. *Journal of Statistical Software* 103, 1–26. doi:10.18637/jss.v103.i07.
- Hubert, L., Arabie, P., 1985. Comparing partitions. *Journal of classification* 2, 193–218.
- Kang, Y., Wu, K., Gao, S., Ng, I., Rao, J., Ye, S., Zhang, F., Fei, T., 2022. STICC: A multivariate spatial clustering method for repeated geographic pattern discovery with consideration of spatial contiguity. doi:10.48550/arXiv.2203.09611.
- Keren, L., Bosse, M., Marquez, D., Angoshtari, R., Jain, S., Varma, S., Yang, S.R., Kurian, A., Valen, D.V., West, R., Bendall, S.C., Angelo, M., 2018. A Structured Tumor-Immune Microenvironment in Triple Negative Breast Cancer Revealed by Multiplexed Ion Beam Imaging. *Cell* 174, 1373–1387.e19. doi:10.1016/j.cell.2018.08.039.
- Kulldorff, M., 1997. A spatial scan statistic. *Communications in Statistics-Theory and methods* 26, 1481–1496.
- Lance, G.N., Williams, W.T., 1967. A General Theory of Classificatory Sorting Strategies: 1. Hierarchical Systems. *The Computer Journal* 9, 373–380. doi:10.1093/comjnl/9.4.373.

- Miranda, L., Filho, J.V., Bernardini, F.C., 2017. RegK-Means: A Clustering Algorithm Using Spatial Contiguity Constraints for Regionalization Problems, in: 2017 Brazilian Conference on Intelligent Systems (BRACIS), pp. 31–36. doi:10.1109/BRACIS.2017.70.
- Muandet, K., Fukumizu, K., Sriperumbudur, B., Schölkopf, B., 2017. Kernel Mean Embedding of Distributions: A Review and Beyond. *FNT in Machine Learning* 10, 1–141. URL: <http://arxiv.org/abs/1605.09522>, doi:10.1561/22000000060. arXiv:1605.09522 [stat].
- Murtagh, F., 1985. A Survey of Algorithms for Contiguity-constrained Clustering and Related Problems. *The Computer Journal* 28, 82–88. doi:10.1093/comjnl/28.1.82.
- Rousseeuw, P.J., 1987. Silhouettes: A graphical aid to the interpretation and validation of cluster analysis. *Journal of Computational and Applied Mathematics* 20, 53–65. doi:10.1016/0377-0427(87)90125-7.
- Schabenberger, O., Gotway, C.A., 2017. Statistical methods for spatial data analysis. Chapman and Hall/CRC.
- Sen, P.K., 1972. Limiting behavior of regular functionals of empirical distributions for stationary*-mixing processes. *Zeitschrift für Wahrscheinlichkeitstheorie und verwandte Gebiete* 25, 71–82.
- Sherman, M., 1996. Variance estimation for statistics computed from spatial lattice data. *Journal of the Royal Statistical Society Series B: Statistical Methodology* 58, 509–523.
- Singhal, V., Chou, N., Lee, J., Yue, Y., Liu, J., Chock, W.K., Lin, L., Chang, Y.C., Teo, E.M.L., Aow, J., Lee, H.K., Chen, K.H., Prabhakar, S., 2024. BANKSY unifies cell typing and tissue domain segmentation for scalable spatial omics data analysis. *Nat Genet* 56, 431–441. doi:10.1038/s41588-024-01664-3.
- Van der Vaart, A.W., 2000. Asymptotic statistics. volume 3. Cambridge university press.
- Yao, J., Yu, J., Caffo, B., Page, S.C., Martinowich, K., Hicks, S.C., 2024. Spatial domain detection using contrastive self-supervised learning for spatial multi-omics technologies. doi:10.1101/2024.02.02.578662.